Supervillin binding to myosin II and synergism with anillin are required for cytokinesis

Tara C. Smith[a], Peter C. Fridy[b], Yinyin Li[c], Shruti Basil[a,*], Sneha Arjun[a,†], Ryan M. Friesen[a,‡], John Leszyk[d], Brian T. Chait[c], Michael P. Rout[b], and Elizabeth J. Luna[a]

[a]Program in Cell and Developmental Dynamics, Department of Cell and Developmental Biology, University of Massachusetts Medical School, Worcester, MA 01655; [b]Laboratory of Cellular and Structural Biology and [c]Laboratory of Mass Spectrometry and Gaseous Ion Chemistry, Rockefeller University, New York, NY 10065; [d]Proteomics and Mass Spectrometry Facility, University of Massachusetts Medical School, Shrewsbury, MA 01545

ABSTRACT **Cytokinesis, the process by which cytoplasm is apportioned between dividing daughter cells, requires coordination of myosin II function, membrane trafficking, and central spindle organization. Most known regulators act during late cytokinesis; a few, including the myosin II–binding proteins anillin and supervillin, act earlier. Anillin's role in scaffolding the membrane cortex with the central spindle is well established, but the mechanism of supervillin action is relatively uncharacterized. We show here that two regions within supervillin affect cell division: residues 831–1281, which bind central spindle proteins, and residues 1–170, which bind the myosin II heavy chain (MHC) and the long form of myosin light-chain kinase. MHC binding is required to rescue supervillin deficiency, and mutagenesis of this site creates a dominant-negative phenotype. Supervillin concentrates activated and total myosin II at the furrow, and simultaneous knockdown of supervillin and anillin additively increases cell division failure. Knockdown of either protein causes mislocalization of the other, and endogenous anillin increases upon supervillin knockdown. Proteomic identification of interaction partners recovered using a high-affinity green fluorescent protein nanobody suggests that supervillin and anillin regulate the myosin II and actin cortical cytoskeletons through separate pathways. We conclude that supervillin and anillin play complementary roles during vertebrate cytokinesis.**

Monitoring Editor
Yu-Li Wang
Carnegie Mellon University

Received: Oct 3, 2012
Revised: Aug 14, 2013
Accepted: Sep 25, 2013

INTRODUCTION

Cytokinesis is a dynamic multistep process in which the plasma membrane, the actin- and myosin II–associated membrane cortex, and components of the microtubule-rich central spindle coordinate the physical separation of a dividing cell into daughter cells (recently reviewed in Green *et al.*, 2012). As animal cells enter anaphase and the central spindle forms, it sends signals that recruit myosin II and actin to the cell equator (Werner *et al.*, 2007; Salbreux *et al.*, 2012). Ingression of the cleavage furrow requires continued myosin II activation at the cell equator and remodeling of the cortical actin cytoskeleton as the furrow narrows into an intracellular bridge with a midbody at its center by telophase (Wang, 2005; D'Avino, 2009). The cortex maintains a close association with the central spindle and midbody until abscission into daughter cells is complete at the end of cytokinesis (Frenette *et al.*, 2012; Green *et al.*, 2012). Successful cell division requires coordination of myosin activation, actin cytoskeletal proteins, and central spindle assembly with membrane trafficking to and from the furrow (Poirier *et al.*, 2012; Salbreux *et al.*, 2012; Schiel and Prekeris, 2013).

Genetic deletion or RNA interference (RNAi)–mediated knockdown of several membrane-associated, cytoskeletal proteins leads to division failure during early cytokinesis. These proteins include myosin II, citron kinase, epithelial cell transforming sequence 2 oncogene (ECT2), epithelial protein lost in neoplasm/LIM domain and actin

This article was published online ahead of print in MBoC in Press (http://www.molbiolcell.org/cgi/doi/10.1091/mbc.E12-10-0714) on October 2, 2013.

Present addresses: *College of Osteopathic Medicine, University of New England, Biddeford, ME 04005; †Drexel University College of Medicine, Philadelphia, PA 19129; ‡Providence Alaska Medical Center, Anchorage, AK 99508.

Address correspondence to: Elizabeth J. Luna (Elizabeth.Luna@umassmed.edu).

Abbreviations used: AnilKD, anillin knockdown by specific double-stranded RNA; bSV, bovine supervillin; ECT2, epithelial cell transforming sequence 2 oncogene; EPLIN/LIMA1, epithelial protein lost in neoplasm/LIM domain and actin binding 1; hSV, human supervillin; L-MLCK, long isoform of myosin light-chain kinase; MHC, myosin II heavy chain; pMRLC, phosphorylated (activated) myosin regulatory light chain; PRC1, protein regulator of cytokinesis 1; SVKD, supervillin knockdown by specific double-stranded RNA.

Supplemental Material can be found at:
http://www.molbiolcell.org/content/suppl/2013/09/30/mbc.E12-10-0714.DC1.html

binding 1 (EPLIN/LIMA1), and two proteins that bind to both myosin II and F-actin: anillin and supervillin (Knecht and Loomis, 1987; Field and Alberts, 1995; Straight *et al.*, 2005; Zhao and Fang, 2005; Chalamalasetty *et al.*, 2006; Gruneberg *et al.*, 2006; Piekny and Glotzer, 2008; Chircop *et al.*, 2009; Smith *et al.*, 2010; Watanabe *et al.*, 2013). After RNAi-mediated depletion of either anillin or supervillin, furrows form and begin to ingress, but then the cells contract and bleb abnormally around their peripheries, with large movements of cytoplasm relative to the cleavage furrow (Straight *et al.*, 2005; Zhao and Fang, 2005; Smith *et al.*, 2010). Vertebrate supervillin and anillin both bind directly to the myosin II heavy chain (MHC) and can bind and bundle actin filaments (Field and Alberts, 1995; Chen *et al.*, 2003; Straight *et al.*, 2005). Anillin and supervillin also both interact with components of the central spindle (Piekny and Glotzer, 2008; Smith *et al.*, 2010; Frenette *et al.*, 2012). In addition, supervillin regulates cell proliferation through control of p53 levels (Fang and Luna, 2013) and contributes to cell motility, invasion, and rapid recycling of membrane vesicles (Crowley *et al.*, 2009; Fang *et al.*, 2010; Bhuwania *et al.*, 2012). These reports suggest overlapping roles for these proteins in regulation of myosin II and actin assembly at the membrane.

Because vertebrate anillin and supervillin both contain binding sites for F-actin, myosin II, and central spindle proteins, we hypothesized that these proteins might play complementary roles in regulating cortex organization relative to the central spindle during early cytokinesis. This hypothesis is consistent with the similarity in timing of cytokinesis failure after knockdown of either protein (Straight *et al.*, 2005; Zhao and Fang, 2005; Smith *et al.*, 2010). Supervillin homologues exist in worms and flies but lack N-terminal sequences corresponding to the myosin II– and actin-binding sites in vertebrate supervillins (Pestonjamasp *et al.*, 1997; Pope *et al.*, 1998; Archer *et al.*, 2005). Thus, reports that loss of anillin from vertebrate cells results in a lower incidence of multinucleated cells than is observed after anillin depletion in *Caenorhabditis elegans* oocytes and *Drosophila* cells (Echard *et al.*, 2004; Maddox *et al.*, 2005; Straight *et al.*, 2005; Zhao and Fang, 2005) may be due to the absence of functionalities specific to vertebrate supervillin.

We further hypothesized that, like anillin (Straight *et al.*, 2005; Zhao and Fang, 2005; Hickson and O'Farrell, 2008; Piekny and Glotzer, 2008), supervillin might promote the localization of activated, phosphorylated myosin regulatory light chain (pMRLC) to the furrow, perhaps through its interactions with the long isoform of myosin light chain kinase (L-MLCK; Takizawa *et al.*, 2007; Bhuwania *et al.*, 2012). Mice lacking MLCK survive to birth, indicating that this protein is dispensable for embryonic cell divisions (Somlyo *et al.*, 2004), but inhibition of MLCK suggests synergy with other kinases during divisions leading to polyploid megakaryocytes (Avanzi *et al.*, 2012). L-MLCK localizes to the cleavage furrow in vertebrates (Poperechnaya *et al.*, 2000), and overexpression of the supervillin-binding L-MLCK N-terminus disrupts cytokinesis (Dulyaninova *et al.*, 2004). We therefore investigated whether supervillin and anillin cooperate during cell division and the role of supervillin and its ability to bind MHC and L-MLCK in this process. We used HeLa cells, in which p53 levels are kept low by papilloma virus proteins in a supervillin-independent pathway (Li *et al.*, 2004; Fang and Luna, 2013), to focus on the role of supervillin's MHC-binding activity during early cytokinesis and how supervillin coordinates with anillin to maintain alignment of the cortical cytoskeleton with the central spindle.

RESULTS

Supervillin regulates myosin II in cell division

We showed previously that the knockdown of supervillin in HeLa cells leads to a significant increase in the number of binucleated and multinucleated cells (Smith *et al.*, 2010). We show here the rescue of that phenotype by expression of enhanced green fluorescent protein (EGFP)–tagged human supervillin (hSV; Figure 1, A–D). This EGFP-hSV message is susceptible to a double-stranded RNA (dsRNA) targeting the coding region of hSV (supervillin knockdown by specific double-stranded RNA-1 [SVKD-1]) but not to a 3′-untranslated region UTR (3′UTR)–targeted dsRNA (SVKD-2; Figure 1A, lanes 5 and 6). EGFP-hSV could not rescue the knockdown phenotype caused by SVKD-1 but reduced to control levels the numbers of binucleated/multinucleated cells generated by SVKD-2 (Figure 1B). Rescue also was observed, with expression levels of EGFP-hSV only twofold to threefold higher than that of endogenous protein in a stable HeLa cell line (Figure 1, C and D), but not by expression of EGFP-tagged bovine supervillin (EGFP–bSV; Figure 1, E and F). Subsequent to this work, we became aware that the EGFP-hSV construct in the stable cell line contains a point mutation (K923E). Nevertheless, both higher levels of wild-type EGFP-hSV (Figure 1, A and B) and near-endogenous levels of EGFP-hSV(K923E) (Figure 1, C and D) rescued the binucleated/multinucleated phenotype of supervillin-knockdown cells.

Two regions of supervillin, including the myosin II regulatory sequence, are important for normal cell division, whereas actin-binding sequences target supervillin to the furrow. Although full-length EGFP-bSV did not rescue the knockdown phenotype, its overexpression was not detectably harmful (Figure 1G). We therefore used a panel of existing EGFP-bSV deletion mutants to determine whether their overexpression would result in dominant-negative increases in binucleated/multinucleated cells in the presence of endogenous hSV (Figure 1G and Supplemental Figures S1 and S2). As compared with EGFP expression alone, cell division was not detectably affected by the expression of bSV-1–171-EGFP or EGFP-bSV-1010–1792. Expression of EGFP-bSV-1–830, which contains the myosin II regulatory sequence plus all three actin-binding sites, caused a small but significant decrease in the number of binucleated/multinucleated cells. By contrast, significant twofold or greater increases in the percentages of binucleated/multinucleated cells were seen upon expression of EGFP-bSV-171–1792, which lacks the myosin II/L-MLCK–binding sequence, and after expression of EGFP-bSV-831–1281, which contains a coiled-coil sequence and binding sites for the central-spindle protein KIF14 and other cell-cycle regulatory proteins (Wulfkuhle *et al.*, 1999; Smith *et al.*, 2010; Figure 1G, red bars). Increases also were observed with other constructs but did not pass statistical testing. Consistent with dominant-negative effects on cell division, we also observed aberrant nuclear and cortical morphologies in cells expressing constructs that increased the numbers of binucleated/multinucleated cells (Supplemental Figure S2, q–t′, y–b″). All constructs that contained the three F-actin–binding sequences within bSV-171–830 (Chen *et al.*, 2003) were concentrated at the furrow (Figure 1G and Supplemental Figure S2). These data suggest that although the myosin II/L-MLCK–interacting region within bSV-1–170 is not required to target supervillin to the furrow of dividing cells, its loss generates a dominant-negative phenotype (Figure 1G).

Supervillin is required for normal localization of total and activated myosin II at the equatorial cortex during cytokinesis (Figure 2). We previously reported that furrow ingression is disrupted after supervillin knockdown and that supervillin promotes myosin II activation at membranes in interphase cells by scaffolding MHC and L-MLCK (Takizawa *et al.*, 2007; Bhuwania *et al.*, 2012). We therefore explored whether supervillin knockdown would displace total or activated myosin II from the cleavage furrow during early cytokinesis (Figure 2), using antibodies against myosin IIA heavy chain

(Figure 2A), the major myosin II isoform in HeLa cells (Maupin *et al.*, 1994), and against phosphorylated Ser-19 in myosin II regulatory light chain (pMRLC; Figure 2B; Matsumura *et al.*, 1998). MHC appearance was indistinguishable from controls through anaphase I (unpublished data). However, compared with controls (Figure 2A, a–d, i–l), myosin II concentrations at the polar cortices increased in supervillin-knockdown cells starting in anaphase II (Figure 2A, e–h, arrowhead) and remained mislocalized through bridge formation (Figure 2A, m–p, arrowheads), resulting in significantly decreased ratios of equatorial-to-polar signals (Figure 2C, red vs. blue regions).

Of interest, the effects of supervillin knockdown on pMRLC localization (Figure 2, B and D) did not follow the same pattern as the effects on total myosin II. Compared to controls (Figure 2B, a–d, i–l), activated myosin II was mislocalized in supervillin-depleted cells in anaphase I (Figure 2B, e–h), regained the expected localization to the invaginating furrow in anaphase II and telophase (Figure 2D), and then became mislocalized again during bridge formation (Figure 2, B, m–p, D). These results suggest that supervillin is required to restrict both total and activated myosin II to the furrow during cell division but is not solely responsible for localizing activated myosin.

Identification of the separate myosin II– and L-MLCK–binding sites

Separate sequences within the supervillin N-terminus interact with myosin II and the L-MLCK N-terminus (Figure 3 and Supplemental Figures S3–S5). Our laboratory showed previously that the N-terminal 174 amino acids of bSV (bSV-1–174) associate with myosin IIB in stress fibers in COS7 cells and cause myosin II to contract into stable punctae containing bSV-1–174-EGFP, MHC, and L-MLCK (Takizawa *et al.*, 2007). We used this system as a first assay for the importance of three well-conserved sequences within bSV-1–174 (Figure 3A, black bars, and Supplemental Figures S3 and S4). As previously shown, cells expressing EGFP alone (Supplemental Figure S3, a–c) displayed normal stress fibers, whereas cells expressing bSV-1–174 tagged with EGFP on either terminus contained punctae of MHC and EGFP (Supplemental Figure S3, d–i). These hypercontractile punctae were eliminated by deletion of either the N-terminal 11 residues or C-terminal 47 amino acids of bSV-1–174 (Figure 3A and Supplemental Figure S3, j–x) and reduced in cells expressing bSV-93–174-EGFP (Supplemental Figure S3, y–a′). Point mutations made in the first two conserved regions had no detectable effect (Supplemental Figure S4, a–o), but charge-to-alanine replacements in the third conserved region (bSV-99–153) either reduced or eliminated the punctae (Supplemental Figure S4, p–x and y–a′, respectively). Taken together, these results implicate the first and third of the three highly conserved sequences within bSV1–174 in supervillin-induced myosin II hypercontractility (Figure 3A).

Our second approach to identifying interaction sites within bSV-1–174 was to sediment EGFP-tagged mutated bSV-1–174 proteins with glutathione *S*-transferase (GST) fusion proteins containing either the subfragment-2 domain of myosin IIA (GST–myo-S2; Figure 3, B–E) or the N-terminal six immunoglobulin (IgG)-like domains of the long isoform of myosin light-chain kinase (GST–L-MLCK; Supplemental Figure S5, A–D). Our laboratory previously showed that GST-bSV-1–174, but not GST alone, binds directly to myosin IIA and IIB S2 domains and to the L-MLCK N-terminus (Chen *et al.*, 2003; Takizawa *et al.*, 2007). In this assay, EGFP-tagged bSV-1–174 bound to each GST construct, as expected (Figure 3, A and B, lane 2, and Supplemental Figure S5A, lane 2). C-terminal deletion of bSV-128–174 (Figure 3, A, B, lanes 4 and 5, and C, lane 3) eliminated binding to GST–myo-S2, but deletion of the first two conserved domains either maintained or enhanced binding (Figure 3, A and B, lanes 6 and 7), suggesting the importance of the third conserved region (bSV99–153) for MHC binding. Point mutagenesis of R107/Y108, R112/R113, R140/K141, and K148/R149 within bSV99–153 also eliminated binding to MHC (Figure 3, C, lanes 5–8, and D, lanes 6 and 7). Binding to GST–myo-S2 was also reduced for bSV-11–174 (Figure 3, A, B, lane 5, and C, lane 4), suggesting that the first conserved region contributes to the binding avidity. However, point mutations within the first two conserved domains did not detectably affect binding to GST–myo-S2 (Figure 3, D, lanes 3–5, and E, lanes 4 and 5).

Results from the GST–L-MLCK pull-down assays showed that the MHC-binding sequence is not required for the interaction with L-MLCK (Figure 3A and Supplemental Figure S5). EGFP-bSV-1–101, which lacks the MHC-binding domain, interacts with GST–L-MLCK (Supplemental Figure S5A, lane 4), and mutations in SV99–153 had no effect on the GST–L-MLCK interaction (Supplemental Figure S5, C, lane 5, and D, lane 6). Interaction with GST–L-MLCK is lost by further deletion of the second domain (EGFP-bSV-1–23; Supplemental Figure S5A, lane 3), but no mutations made in the first two conserved domains eliminated the interaction (Supplemental Figure S5, B, lane 3, C, lanes 3 and 4, and D, lane 4). We considered the possibility that myosin IIA might be acting as a bridge between GST–L-MLCK and bSV-1–174-EGFP in the pull-down assays, thereby masking the effectiveness of the point mutants. However, the GST-tagged L-MLCK bait lacks the MHC-binding site in the L-MLCK C-terminus, and endogenous MHC is absent from relevant bound fractions (Supplemental Figure S5E). These results show that our assay design precluded recovery of significant amounts of the ternary complex of bSV-1–174 with MHC and L-MLCK. They also show that the L-MLCK interaction site within the supervillin N-terminus is distinct from the binding site for MHC.

The sequences within supervillin investigated here are highly conserved among vertebrates (Figure 3F). The first conserved region within bSV1–174 contributes to, but is not required for, binding to both MHC and L-MLCK. The second conserved region may be part of a larger site involved in L-MLCK binding. The first and third sequences are both required for supervillin-induced myosin II hypercontractility (Figure 3A, black bars, and Supplemental Figure S3). The third conserved domain also is essential for binding to MHC, with numerous point mutations (Figure 3F, brackets labeled M), supporting the results of deletion analyses. Because the R140A,K141A mutation effectively abolished both MHC binding and the generation of hypercontractile punctae in the COS7 experiments (Figure 3, A and C, and Supplemental Figure 4), we chose it for further experiments.

Myosin II binding is important for supervillin function during cell division

Supervillin proteins with point mutations at the MHC-binding site exhibit dominant-negative effects on cell division and are unable to rescue the supervillin-knockdown phenotype (Figure 4). To further test the requirement of the supervillin–myosin II interaction for cytokinesis, we transferred point mutations into full-length EGFP-bSV and repeated the assay for dominant-negative effects on cell division in the presence of endogenous supervillin, using EGFP alone and bSV-171–1792 as controls (Figure 4A). Point mutations in the first two conserved domains did not significantly affect the percentages of binucleate/multinucleate cells (Figure 4A; K4A, R6A, R9A, R10A and E36A, E37A). By contrast, the R140A,K141A mutation, which eliminated MHC binding in vitro and in vivo (Figure 3 and Supplemental Figure S4), was as effective as bSV-171–1792 at inducing a

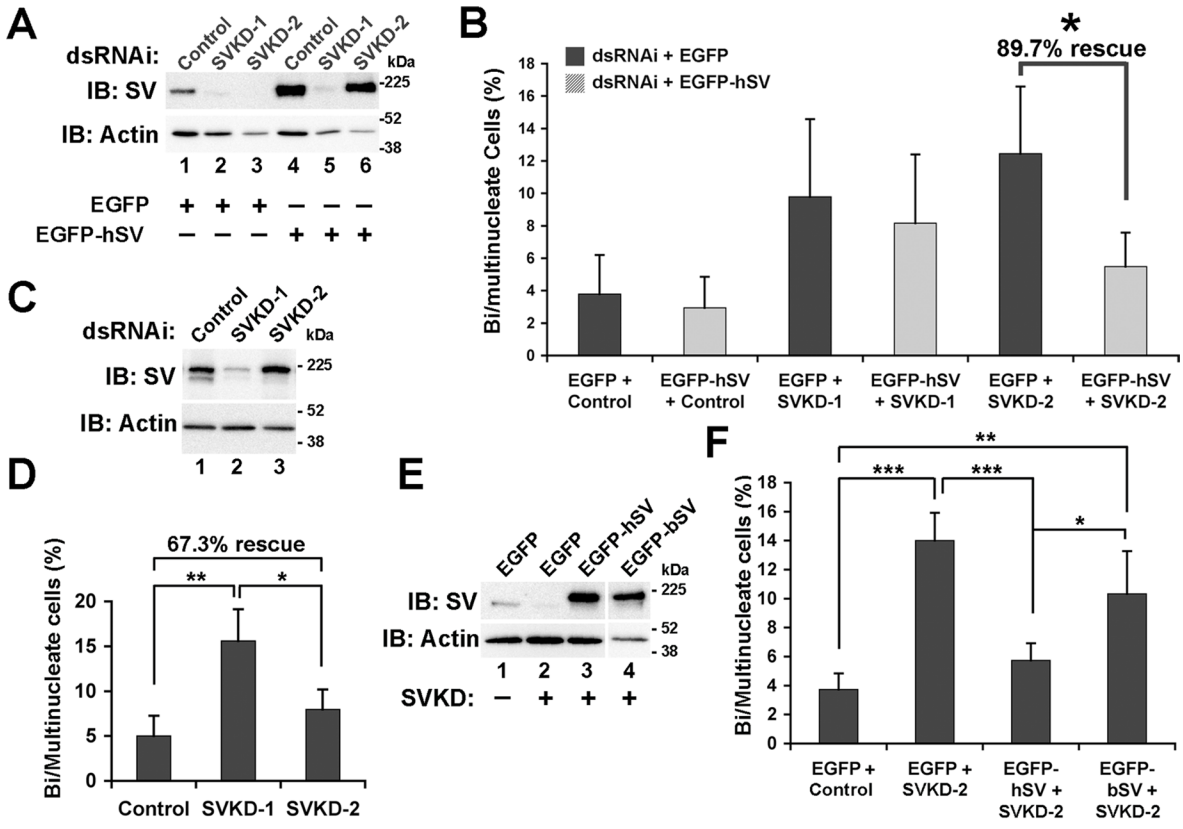

G

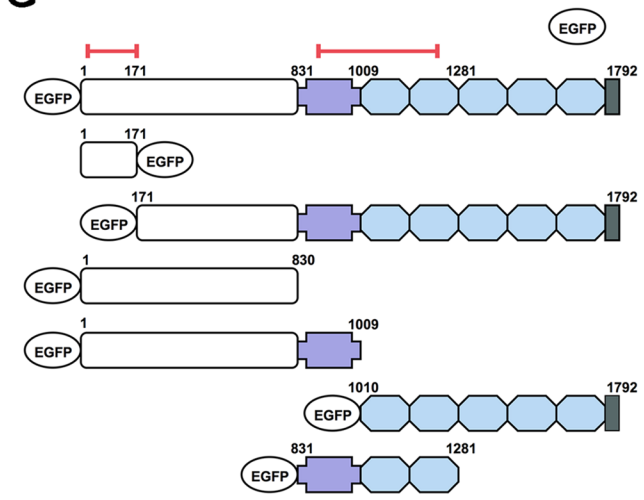

	Fold change in binucleate cells	Total cells (# expts)	Localization during division
EGFP	1.00	747 (9)	Diffuse, Midbody
EGFP-hSV	1.09 + 0.79	254 (4)	Furrow
EGFP-bSV	1.02 + 0.42	350 (4)	Diffuse, Midbody
EGFP-hSV(1–171)	2.04 + 0.44	281 (4)	Furrow
EGFP-hSV(1–830)	0.81 + 0.04	220 (3)	Furrow
EGFP-hSV(1–1009)	2.35 + 1.36	172 (5)	Furrow
EGFP-hSV(1010–1792)	0.94 + 0.47	234 (3)	Diffuse, Midbody
EGFP-hSV(831–1281)	2.15 + 0.92	209 (6)	Diffuse, Midbody

FIGURE 1: Overexpressed EGFP-hSV, but not EGFP-bSV, rescues the increase in binucleated/multinucleated cells caused by knockdown of supervillin; key roles for residues 1–171 and 831–1281 are suggested by dominant-negative effects of EGFP-bSV deletion proteins. (A) Immunoblots showing knockdown of endogenous supervillin and overexpression of EGFP-hSV; actin used as loading control. Lanes 1–3, EGFP with control (1), SVKD-1 (2), or SVKD-2 (3) dsRNAs; lanes 4–6, EGFP-hSV with control (4), SVKD-1 (5), or SVKD-2 (6) dsRNAs. (B) Quantification of binucleated/multinucleated HeLa cells simultaneously transfected with EGFP (black bars) or EGFP-hSV (gray bars) and dsRNAs, as indicated. EGFP-hSV is immune to the SVKD-2 dsRNA. Means ± SD; $N = 3$; *$p = 0.0424$ (paired two-tailed t test). (C) Immunoblots and (D) quantification of binucleated/multinucleated HeLa cells stably expressing EGFP-hSV(K923E) after transfection with 20 nM dsRNAs, as indicated. Means ± SD; $N = 4$; *$p = 0.0103$, **$p = 0.0025$ (paired two-tailed t test). (E) Immunoblots and (F) quantification of binucleated/multinucleated HeLa cells cotransfected with EGFP constructs and either control or SVKD-2 dsRNA, as indicated in E. Means ± SD; $N = 4$, >50 cells counted per condition per experiment; *$p < 0.05$, **$p < 0.01$, ***$p < 0.001$ (analysis of variance [ANOVA]). (G) Fold increase (dominant-negative effect) of binucleated/multinucleated HeLa cells after expression of the indicated EGFP-tagged bSV deletion mutants for 48 h (representative images in Supplemental Figure S1) and the localizations of these proteins during cell division (Supplemental Figure S2). Columns show means ± SD, relative to EGFP-transfected cells;

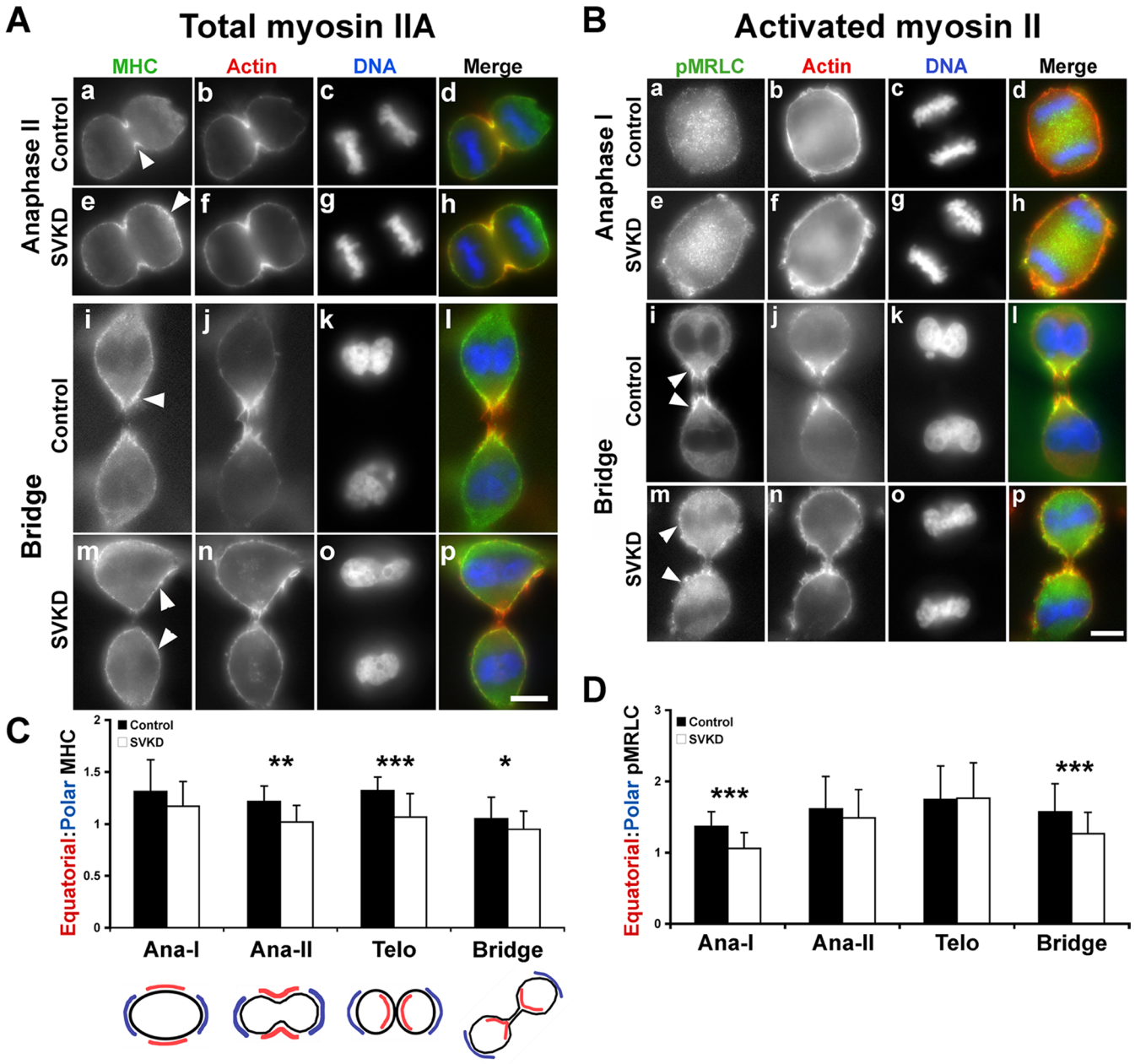

FIGURE 2: Supervillin is required for localization of myosin II at the cytokinetic furrow. (A, B) Immunofluorescence localizations of (A) total MHC and (B) regulatory myosin II light chain phosphorylated at Ser-19 (pMRLC, active myosin II) in synchronized HeLa cells transfected with control (a–d, i–l) or supervillin-specific (SVKD-2; e–h, m–p) dsRNA. MHC or pMRLC signal (a, e, i, m; green in merges); F-actin (b, f, j, n; red in merges), DNA (c, g, k, o; blue in merges) in dividing cells. White arrowheads, MHC and pMRLC localizations. Bars, 10 μm. (C, D) Mean ratios of cortex-specific equatorial (red) to polar (blue) total (C) and activated myosin II (D) signals in cells at different stages; *$p = 0.0483$, **$p = 0.0058$, ***$p \leq 0.0007$ (two-tailed t test). Black bars, control cells; white bars, SVKD-2 cells. Number of cells analyzed was as follows: (C) anaphase I ($N = 8$ control, 13 SVKD), anaphase II ($N = 12$ control, 11 SVKD), telophase ($N = 13$ control, 23 SVKD), and cytokinesis ($N = 29$ control, 30 SVKD), $N = 2$ experiments; and (D) anaphase I ($N = 15$ control, 13 SVKD), anaphase II ($N = 19$ control, 24 SVKD), telophase ($N = 13$ control, 30 SVKD), and cytokinesis ($N = 38$ control, 44 SVKD), $N = 5$ experiments.

total numbers of cells and experiments; and localizations of deletion proteins in dividing cells. Red boxes denote statistically significant effects on cell division ($p \leq 0.05$, two-tailed t test). Red brackets, regions implicated as important for cytokinesis, either when absent (bSV1–171) or overexpressed (bSV831–1281). Supervillin domains are shown as (white) the intrinsically disordered N-terminus (Fedechkin *et al.*, 2013), (purple) the central region with a predicted coiled-coil domain (Wulfkuhle *et al.*, 1999), (blue) five sequences with homology to gelsolin repeats (Pestonjamasp *et al.*, 1997), and (gray) the C-terminus with structural similarity to the villin headpiece (Vardar *et al.*, 2002).

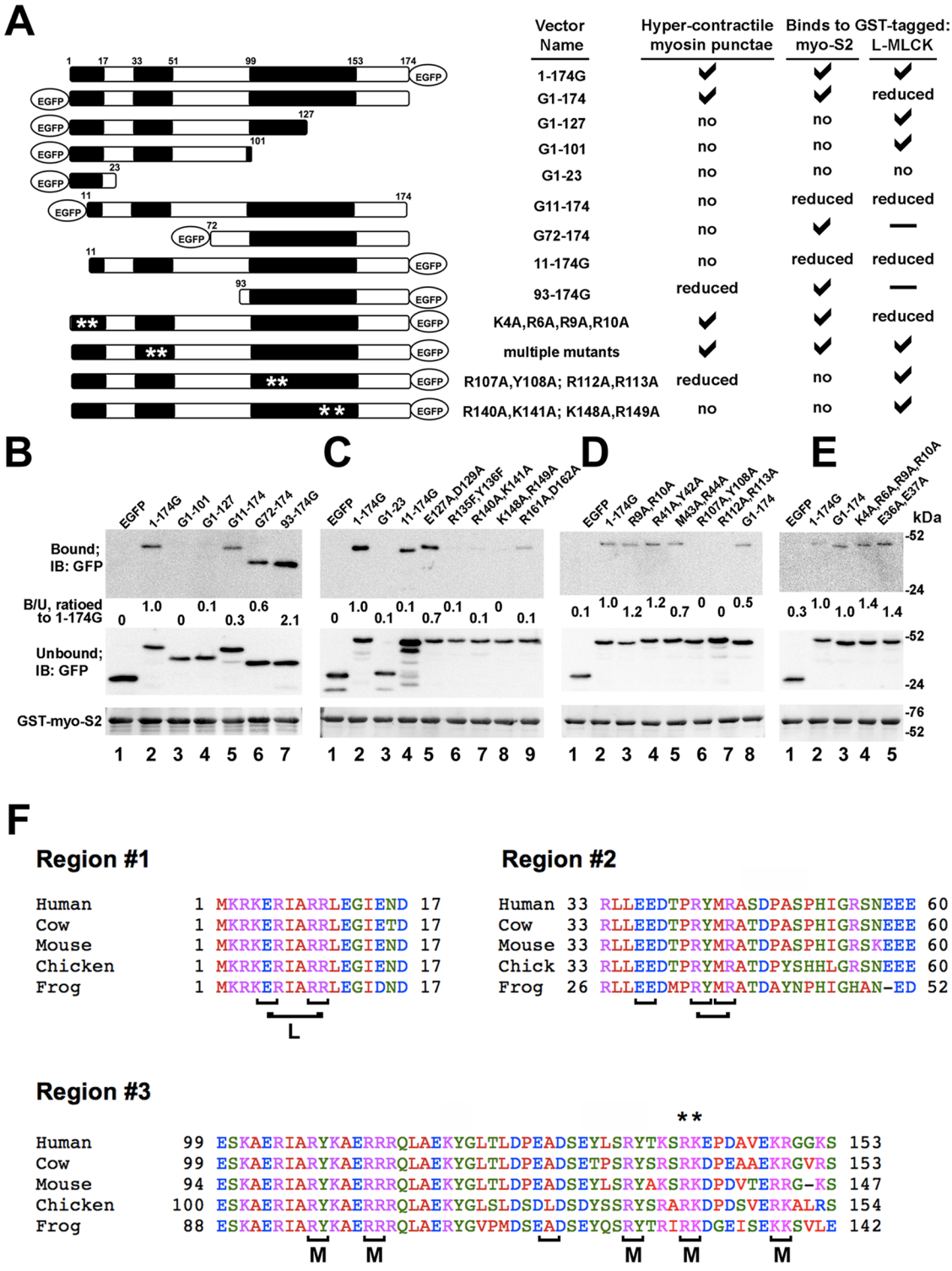

FIGURE 3: Deletion and point mutagenesis of the myosin II–binding site. (A) Summation of results with EGFP-tagged deletion and point mutants of bovine SV1–174 obtained from in vivo overexpression experiments in COS7 cells (hypercontractile myosin punctae; Supplemental Figures S3 and S4) and from pull-down experiments with GST-tagged myosin II S2 (GST–myo-S2) or GST-tagged L-MLCK N-terminus (GST–L-MLCK; Supplemental Figure S5). Highly conserved regions in SV1–174 are indicated in black. White asterisks show approximate locations of point mutations. (B–E) Representative anti-GFP immunoblots of bound and unbound GFP-tagged SV1–174 mutant proteins, as indicated, after pull down with GST–myo-S2. Ratios show the bound-to-unbound GFP signals as a fraction of the SV1–174-EGFP signal (positive control). $N \geq 2$. Ratios ≤0.5 were considered binding reductions (A, reduced) and ratios ≤0.1 as no binding to myosin II (A, no). Ponceau-stained blots of bound proteins show levels of GST–myo-S2. (F) Sequences of highly conserved regions within supervillin amino acids 1–174. Amino acid sequences from human (*Homo sapiens*, NP_003165), cow (*Bos taurus*, NP_776615), mouse (*Mus musculus*, ADP02396.1), chicken (*Gallus gallus*, XP_418577.3),

dominant-negative defect in cytokinesis (Figure 4A). We then performed rescue experiments after mutating the same myosin II–affecting residues in the full-length EGFP-tagged human supervillin (Figure 4B). Wild-type supervillin (EGFP-hSV) again rescued the knockdown phenotype, but two mutants defective in binding to MHC (R140A,K141A; K148A,R149A; Figure 3C, lanes 7 and 8) failed to return the numbers of binucleate/multinucleate cells to control levels. Although these experiments do rule out a role for the supervillin interaction with L-MLCK during cytokinesis, they show that the interaction with myosin II is critical for normal cell division.

Supervillin and anillin play nonredundant roles in cell division

Supervillin and anillin are both required for high-fidelity production of daughter cells (Figure 5). The phenotypes observed upon supervillin knockdown are similar to that of another cortical cell division protein, anillin, which also is required for the localization of total and active myosin II at the cleavage furrow (Straight *et al.*, 2005; Zhao and Fang, 2005). Although their amino acid sequences are very different, supervillin and anillin exhibit a similar organization of interaction domains: both bind directly to myosin II and F-actin, contain functional nuclear targeting sequences (Figure 5A, black T), and are predicted to have a central coiled-coil domain (Figure 5A, blue bars; Pope *et al.*, 1998; Wulfkuhle *et al.*, 1999; Oegema *et al.*, 2000; Chen *et al.*, 2003; Straight *et al.*, 2005; Piekny and Glotzer, 2008). Both also bind to proteins in the central spindle: anillin to citron kinase, RhoA, and the RhoA guanine nucleotide exchange factor ECT2 (Piekny and Glotzer, 2008; Gai *et al.*, 2011; Frenette *et al.*, 2012), and supervillin to the kinesin KIF14 and to protein regulator of cytokinesis 1 (PRC1; Zhu *et al.*, 2005; Carleton *et al.*, 2006; Gruneberg *et al.*, 2006; Smith *et al.*, 2010; Hasegawa *et al.*, 2013). In addition, the supervillin C-terminus binds to the furrow-regulatory protein, EPLIN (Chircop *et al.*, 2009; Smith *et al.*, 2010). To determine the relationship between supervillin and anillin during cell division, we first quantified the effects on HeLa cell division after single and double knockdowns of these two proteins. The numbers of binucleated/multinucleated cells increased significantly (Figure 5, B, white arrowheads, and C) after the knockdown of either supervillin alone (Figure 5B, b, SVKD) or anillin alone (Figure 5, B, c and e; anillin knockdown by specific double-stranded RNA-1 [AnilKD-1], AnilKD-2), as compared with treatment with control dsRNA (Figure 5, B, a, and C). Knockdown efficiency (Figure 5D) and percentage increase in number of binucleated cells for single knockdowns were similar to those reported previously (Straight *et al.*, 2005; Zhao and Fang, 2005; Smith *et al.*, 2010). Supervillin levels were unaffected by anillin knockdown, but surprisingly the amount of endogenous anillin increased an average of (1.9 ± 0.3)-fold (both dsRNAs, $n = 11$; $p < 0.0001$, *t* test) after supervillin knockdown (Figure 5D, lane 2). Simultaneous knockdown of supervillin and anillin approximately doubled the percentages of binucleated/multinucleated cells as compared with either single knockdown, with up to ~80% of cells failing cytokinesis (Figure 5, B, d and f, and C). These effects were more than additive, consistent with effects in parallel pathways.

We next asked whether overexpression of EGFP-hSV could rescue the binucleate phenotype caused by knockdown of anillin (Figure 5, E and F). We simultaneously transfected HeLa cells with either control or anillin-specific dsRNAs and a plasmid encoding either EGFP alone or EGFP-hSV (Figure 5, E and F); we also used the HeLa cell line that stably expresses EGFP-hSV(K923E) (unpublished data). In both cases, the percentages of binucleate cells upon anillin knockdown were unaffected by the overexpression of supervillin (Figure 5E). Knockdown of anillin and expression of both EGFP and EGFP-hSV were confirmed by Western blot (Figure 5F). We also made several attempts at the reciprocal experiment, to rescue supervillin knockdown by overexpression of EGFP-anillin, but were unsuccessful due to an apparent loss of substrate adhesion by cells expressing EGFP-anillin for >24 h. In this context, we note that the nearly twofold increase of endogenous anillin that occurs in supervillin-knockdown cells (Figure 5D) is insufficient to fully block the effects of supervillin knockdown (Figure 5C). However, partial compensation by increased anillin may explain why the binucleate/multinucleate phenotype caused by knockdown of supervillin alone

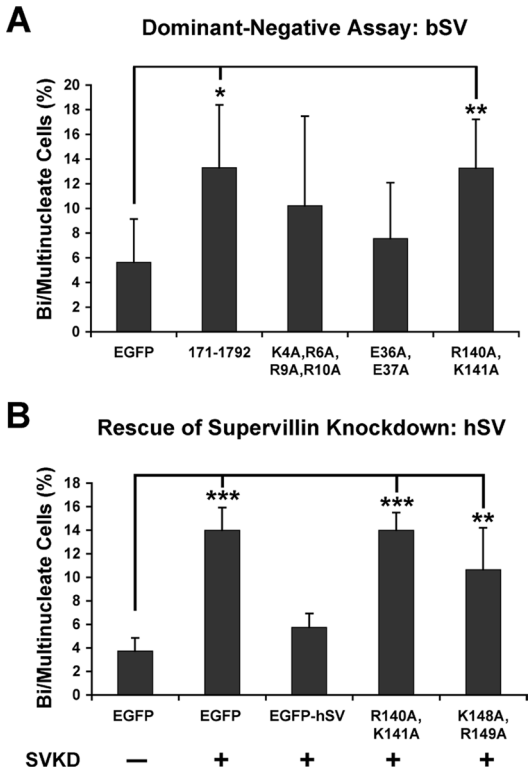

FIGURE 4: Point mutations that disrupt binding to myosin II mimic the dominant-negative phenotype of bSV171–1792 and eliminate rescue of the binucleate/multinucleate phenotype by full-length human EGFP-SV. (A) Dominant-negative overexpression of EGFP-bSV constructs. Cells were assayed as in Figure 1G. Means ± SD; $N \geq 3$ experiments; >30–151 cells per condition per experiment. *p = 0.0228, **p = 0.0055 (paired two-tailed *t* test). (B) Lack of rescue of the binucleate/multinucleate phenotype in SVKD cells by EGFP-hSV proteins containing point mutations that eliminate myosin II binding (hSV-R140A,K141A; hSV-K148A,R149A). Mean percentages of binucleate/multinucleate cells ± SD; $N \geq 3$ experiments; ≥60 cells counted per condition per experiment. **$p < 0.01$, ***$p < 0.001$ (ANOVA).

and frog (*Xenopus* (*Silurana*) *tropicalis*, NP_001090765.1) supervillins were aligned using CLUSTALW 2.1 (www.genome.jp/tools/clustalw/). Brackets, residues targeted for alanine or phenylalanine replacement, as described in *Materials and Methods*. L, the four-residue mutation that reduced the L-MLCK interaction; M, mutations that reduced or eliminated myosin II interaction. **Point mutation used in subsequent assays.

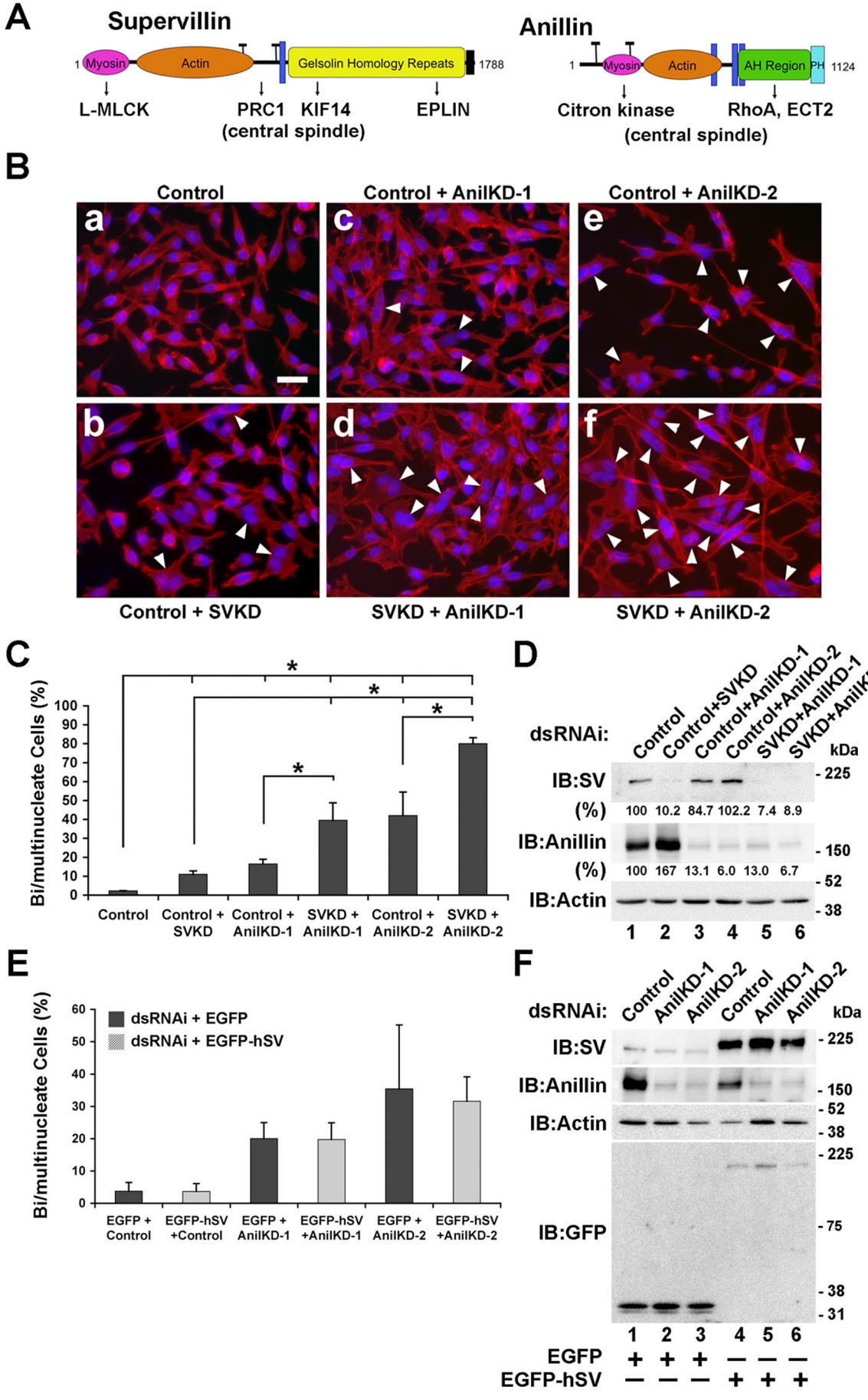
A
Supervillin
1
Myosin
Actin
Gelsolin Homology Repeats
1788
L-MLCK
PRC1
(central spindle)
KIF14
EPLIN
Anillin
1
Myosin
Actin
AH Region
PH
1124
Citron kinase
(central spindle)
RhoA, ECT2
B
Control
Control + AnilKD-1
Control + AnilKD-2
a
c
e
b
d
f
Control + SVKD
SVKD + AnilKD-1
SVKD + AnilKD-2
C
Bi/multinucleate Cells (%)
100
90
80
70
60
50
40
30
20
10
0
*
*
*
*
Control
Control + SVKD
Control + AnilKD-1
SVKD + AnilKD-1
Control + AnilKD-2
SVKD + AnilKD-2
D
dsRNAi:
Control
Control+SVKD
Control+AnilKD-1
Control+AnilKD-2
SVKD+AnilKD-1
SVKD+AnilKD-2
kDa
IB:SV
- 225
(%)
100 10.2 84.7 102.2 7.4 8.9
IB:Anillin
- 150
(%)
100 167 13.1 6.0 13.0 6.7
- 52
IB:Actin
- 38
1 2 3 4 5 6
E
Bi/multinucleate Cells (%)
60
50
40
30
20
10
0
dsRNAi + EGFP
dsRNAi + EGFP-hSV
EGFP + Control
EGFP-hSV +Control
EGFP + AnilKD-1
EGFP-hSV +AnilKD-1
EGFP + AnilKD-2
EGFP-hSV +AnilKD-2
F
dsRNAi:
Control
AnilKD-1
AnilKD-2
Control
AnilKD-1
AnilKD-2
kDa
IB:SV
- 225
IB:Anillin
- 150
- 52
IB:Actin
- 38
- 225
IB:GFP
- 75
- 38
- 31
1 2 3 4 5 6
EGFP + + + — — —
EGFP-hSV — — — + + +

is less penetrant than that seen in anillin-depleted cells (Figure 5C) and raises the possibility of intersecting pathways.

Supervillin is mislocalized in dividing cells depleted of anillin. To determine where and when supervillin and anillin pathways might cross-talk during cell division, we first used the HeLa stable cell line from Figure 1D to quantify supervillin localization in cells depleted of anillin (Figure 6). Consistent with our previous observation with bovine supervillin (Smith *et al.*, 2010), human supervillin concentrated at the cleavage furrow in cells treated with control dsRNA (Figure 6A, a–h′). The equatorial-to-polar ratio of supervillin in these control cells increased during anaphase II and telophase, dropping somewhat at bridge formation (Figure 6B, black bars). By contrast, anillin knockdown mislocalized supervillin away from the cleavage furrow by anaphase II (Figure 6A, i–p′ and q–x′, white arrowheads), as represented by a relatively constant equatorial-to-polar ratio of supervillin signals throughout cell division (Figure 6B, gray and white bars). Note that anillin-depleted cells generally do not progress past anaphase II before furrowing fails (Straight *et al.*, 2005; Zhao and Fang, 2005), making it impossible to determine whether supervillin can be recruited to the membrane around the midbody in late cytokinesis (Smith *et al.*, 2010) after anillin knockdown.

Anillin localization is independent of supervillin from anaphase through telophase (unpublished data) but becomes mislocalized in supervillin-knockdown cells away from the midbody and into the cortices of the bridge and nascent daughter cells (Figure 7). Consistent with previous reports (Field and Alberts, 1995; Oegema *et al.*, 2000), anillin concentrates at the center of the midbody within the cytokinetic bridge in dividing HeLa cells treated with control dsRNA (Figure 7, A, a–d′, white arrowheads, and B, red box). However, in supervillin-knockdown cells, anillin became redistributed away from the midbody into the cortices of the daughter cells at the proximal ends of the cytokinetic bridge (Figure 7, A, e–h′ and i–l′, white arrowheads, and B, blue region). This aberrant anillin signal is reminiscent of both the supervillin (Smith *et al.*, 2010) and myosin II (Figure 2Ai) localizations in control cells at this stage of cell division. This localization also resembles that observed for anillin after knockdown of the central spindle component citron kinase (Gai *et al.*, 2011). Taken together with the mislocalization of supervillin upon loss of anillin (Figure 6), these results suggest compensatory pathways that may cross-talk to regulate myosin II activity during cell division.

Overlapping cytoskeletal interactors but distinct signaling proteins

Protein affinity isolations suggest overlapping cytoskeletal partners and distinct signaling pathways for supervillin and anillin (Table 1). We used a high-affinity anti-GFP nanobody on magnetic beads (Domanski *et al.*, 2012) to collect complexes from extracts of HeLa cells that were transfected for 24 h with EGFP alone, EGFP-tagged hSV, or EGFP-tagged anillin. Cultures were enriched for dividing cells by treating with a Cdk1 inhibitor to synchronize them at the G2/M boundary; unsynchronized cells were used for comparison. Bead-associated proteins were eluted and identified by mass spectrometry using stringent criteria for protein assignments. The most abundant interacting proteins specific for supervillin and anillin are shown in Table 1. Nonspecific contaminants were defined as proteins that were represented by total spectral peptide counts in the EGFP-only samples that were ≥50% of those observed in the EGFP-supervillin or EGFP-anillin samples (Supplemental Table S2). The majority of these contaminants were skin epithelial proteins, but they included abundant proteins from many intracellular compartments. All proteins specifically recovered with GFP nanobody beads from M-phase–enriched and unsynchronized cells are listed in Supplemental Tables S3 and S4, respectively. Although supervillin and anillin did not appreciably coisolate with each other, myosin II was the most abundant specific interactor for each, with both the myosin IIA heavy chain (MYH9) and light chains well represented (Table 1). Actin and actin-binding proteins, such as filamin A, also are abundant in the pull downs for both proteins.

Additional known interactors for each protein are well represented in our affinity isolations (Table 1). These include the supervillin interactors, EPLIN, KIF14, and 14-3-3 proteins (Jin *et al.*, 2004; Smith *et al.*, 2010). All three of these proteins participate in signaling pathways that, like supervillin, regulate both cell motility and cytokinesis (Carleton *et al.*, 2006; Gruneberg *et al.*, 2006; Han *et al.*, 2007; Chircop *et al.*, 2009; Zhou *et al.*, 2010; Freeman and Morrison, 2011; Ahmed *et al.*, 2012). Anillin-specific interacting proteins include CD2AP, SH3KBP1/CIN85/Cindr, and citron Rho-interacting kinase (Table 1; Monzo *et al.*, 2005; Haglund *et al.*, 2010; Gai *et al.*, 2011). CD2AP and SH3KBP1 are SH3 domain–containing proteins that participate in membrane trafficking and actin remodeling, as well as cytokinesis (Monzo *et al.*, 2005; Havrylov *et al.*, 2008; Johnson *et al.*,

FIGURE 5: Supervillin (SV) and anillin synergistically regulate cell division, but supervillin overexpression does not rescue anillin knockdown. (A) Similar organization of binding sites in supervillin and anillin. Both proteins bind directly to myosin II (pink), bind and bundle F-actin (orange), and contain nuclear localization signals (black T's) and coiled-coil domains (dark blue). Both bind central spindle proteins: supervillin to PRC1 and KIF14, which also binds citron kinase; and anillin to citron kinase, RhoA, and the Rho guanine nucleotide exchange factor ECT2. The supervillin N-terminus also binds to L-MLCK, and its C-terminus interacts with EPLIN/LIMA1, another cytokinetic regulator. Gelsolin homology repeats (yellow); villin-like headpiece (black bar); anillin homology region (AH, green); PH domain (cyan). (B) Representative micrographs of each knockdown condition showing binucleated/multinucleated HeLa cells (white arrowheads). (a) Control, (b) control + SV knockdown (SVKD-2), (c) control + anillin knockdown 1 (AnilKD-1), (d) SVKD-2 + AnilKD-1, (e) control + anillin knockdown 2 (AnilKD-2), and (f) SVKD-2 + AnilKD-2. Actin shown in red, DNA in blue. Bar, 20 μm. (C) Percentages of cells with two or more nuclei 48 h after transfection with control, supervillin-specific, or anillin-specific dsRNAs. Means ± SD, $n > 250$ cells counted per condition per experiment; $N = 3$ experiments; $^*p < 0.05$ (paired two-tailed *t* test). (D) Immunoblots of HeLa lysates showing supervillin and anillin knockdowns (20 nM total dsRNA), with actin as loading control. Numbers indicate the mean residual percentages of supervillin and anillin after 48 h of knockdown, $N = 4$. Endogenous anillin levels consistently increased at 48 h in supervillin-knockdown cells. Lanes: 1, control dsRNA; 2, control + SVKD-2; 3, control + AnilKD-1; 4, control + AnilKD-2; 5, SVKD-2 + AnilKD-1; 6, SVKD-2 + AnilKD-2. (E) Quantification of binucleated/multinucleated HeLa cells simultaneously transfected with EGFP (black bars) or EGFP-hSV (gray bars) and anillin dsRNAs, as indicated. Means ± SD; $N = 3$ experiments, >46–143 cells counted per condition per experiment. (F) Immunoblots showing overexpression of EGFP-hSV and knockdown of anillin; actin used as loading control. Anti-GFP confirms expression of EGFP and EGFP-hSV. Lanes 1–3, EGFP with control (1), Anil KD-1 (2), or Anil KD-2 (3) dsRNAs; lanes 4–6, EGFP-hSV with control (4), Anil KD-1 (5), or Anil KD-2 (6) dsRNAs.

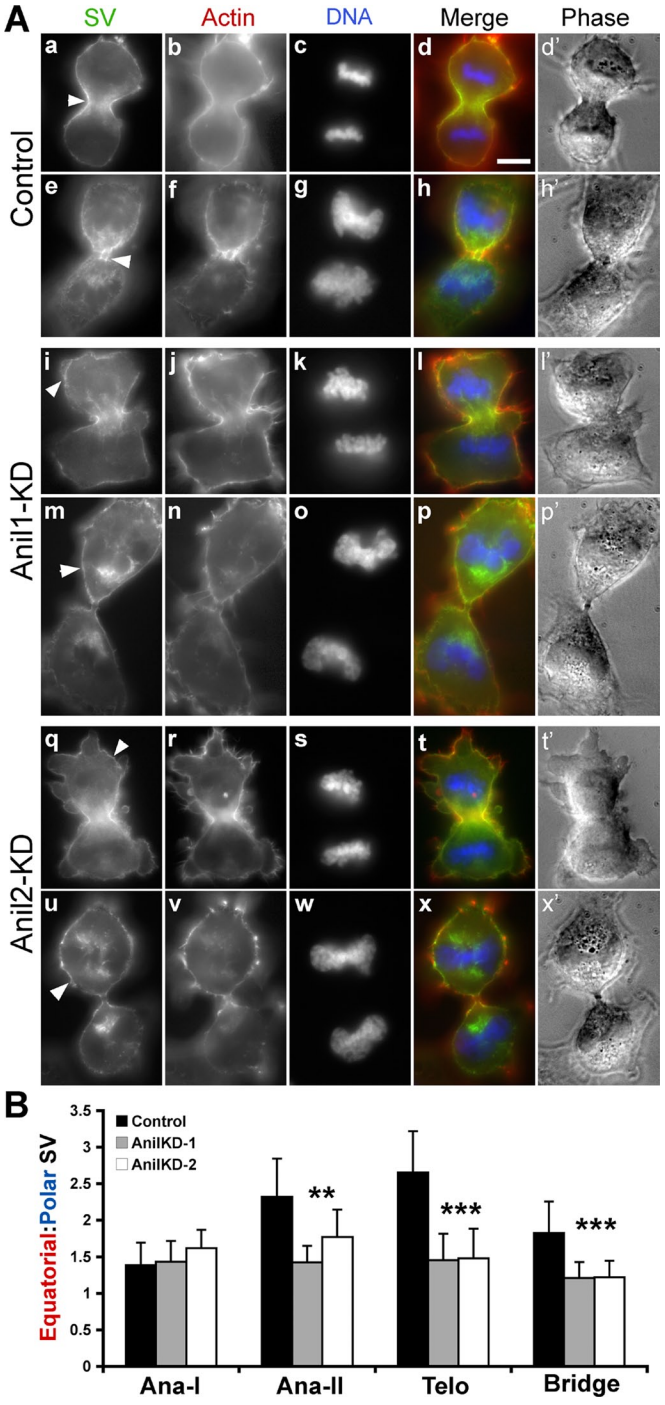

FIGURE 6: Supervillin remains at the furrow during initial stages of division in anillin-knockdown cells but becomes mislocalized in late anaphase. (A) HeLa cells stably expressing EGFP-hSV(K923E) were transfected with either control (a–h′) or one of two anillin-specific dsRNAs (i–x′), and stained with anti-EGFP (a, e, i, m, q, u; green in merge), actin (b, f, j, n, r, v; red in merge), and DNA (c, g, k, o, s, w; blue in merge). Phase images shown in d′, h′, l′, p′, t′, x′. Bar, 10 μm. Supervillin is initially present at the invaginating furrow in dividing cells but becomes mislocalized around the cortex beginning in anaphase II in anillin-knockdown cells (white arrowheads in e, i, m, q, u). (B) Ratio of cortex-specific equatorial-to-polar SV signal in cells at indicated stages of cell division, calculated as in Figure 2; $^{**}p < 0.01$, $^{***}p < 0.001$ (ANOVA). Black bars, control cells; gray bars, AnilKD-1 cells; white bars, AnilKD-2 cells. Numbers of cells analyzed at each stage, combined from two different experiments: anaphase I ($N = 7$ control, 13 Anil1, 6 Anil2), anaphase II ($N = 8$ control, 16 Anil1, 15 Anil2), telophase ($N = 5$ control, 12 Anil1, 15 Anil2), and cytokinesis ($N = 23$ control, 22 Anil1, 11 Anil2).

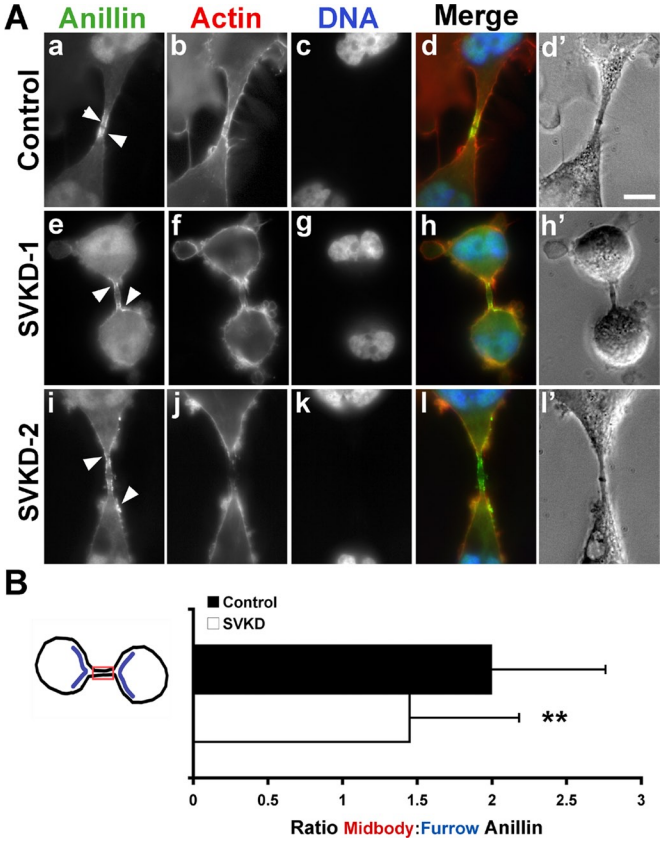

FIGURE 7: Anillin is mislocalized away from the midbody into the cortex during cytokinesis in supervillin-knockdown cells. (A) HeLa cells transfected with control (a–d′) or supervillin-specific (SVKD-1, e–h′; SVKD-2, i–l′) dsRNAs and stained for endogenous anillin (a, e, i; green in merge), actin (b, f, j; red in merge), and DNA (c, g, k; blue in merge). Phase images shown in d′, h′, l′. Bar, 10 μm. Anillin localization at the midbody and cytokinetic furrow shown by white arrowheads (a, e, i). (B) Ratio of anillin signal in the midbody (red box) vs. the cortices of the daughter cells proximal to the furrow (blue). Mean ratios ± SD; $N = 3$ experiments; $^{**}p = 0.0019$ (two-tailed t test). Total number of cells assayed: 34 control (black bar) and 77 SVKD (white bar).

2008; Samoylenko *et al.*, 2012), and citron kinase regulates cytokinesis through its interactions with Rho and KIF14 (Gruneberg *et al.*, 2006; Watanabe *et al.*, 2013). The presence of citron kinase in only the isolates from synchronized EGFP-anillin cells suggests that the enrichment for M-phase cells was effective. By contrast, supervillin-interacting proteins appear to be largely the same in interphase versus M-phase and include many proteins (α-actinin, capping protein, tropomyosin, tropomodulin) associated with stress fibers and other unbranched actin filaments.

Many new candidate interactors for supervillin and anillin also were revealed (Table 1 and Supplemental Tables S3 and S4). Novel direct or indirect interactors for supervillin include four membrane-associated myosins (myosins 1B, 1C, 6, and 18A), suggesting additional loci for cross-regulation of membrane dynamics and furrow structure. Supervillin family members flightless-1 and gelsolin also emerged as supervillin-selective interactors (Table 1). Flightless-1

	Total spectral counts (minus background)					
	M phase		Unsynchronized		Known interactors	
Protein	SVIL	ANLN	SVIL	ANLN	Supervillin	Anillin
Myosin II						
Myosin-9, MYH9	1480	180	1449	515	Chen *et al.* (2003)	Straight *et al.* (2005)
Myosin regulatory light chain 12A, MYL12A	55	6	67	21		
Myosin light polypeptide 6, MYL6	33	3	46	6		
Myosin regulatory light polypeptide 9, MYL9	39	0	41	0		
Baits						
Supervillin, SVIL	993	0	2182	0		
Anillin, ANLN	11	1300	7	1946		
Other myosins						
Unconventional myosin-Ic, MYO1C	156	10	209	47		
Unconventional myosin-Ib, MYO1B	154	5	200	29		
Unconventional myosin-VI, MYO6	150	1	214	15		
Unconventional myosin-XVIIIa, MYO18A	100	0	30	0		
Actin and actin-binding proteins						
Actin, cytoplasmic 2, ACTG1	603	49	1175	148		
Actin, cytoplasmic 1, ACTB	607	68	1175	164	Chen *et al.* (2003)	Field and Alberts (1995)
Filamin-A, FLNA	80	65	110	19	Smith *et al.* (2010)	
α-Actinin-4, ACTN4	117	14	161	33	Nebl *et al.* (2002)	
α-Actinin-1, ACTN1	71	12	96	15	Nebl *et al.* (2002)	
F-actin-capping protein subunit α-1, CAPZA1	86	34	124	106		
F-actin-capping protein subunit α-2, CAPZA2	51	14	58	51		
F-actin-capping protein subunit β, CAPZB	87	17	99	114		
Coronin-1C, CORO1C	82	8	135	23		
Drebrin, DBN1	81	0	49	9		
Protein flightless-1 homologue, FLII	48	0	33	0		
Gelsolin, GSN	30	1	8	0		
LIM domain and actin-binding protein 1, LIMA1/EPLIN	25	0	82	0	Smith *et al.* (2010)	
Tropomyosin α-1 chain, TPM1	40	0	33	5		
Tropomyosin β chain, TPM2	34	0	25	4		
Tropomyosin α-3 chain, TPM3	42	0	30	5		
Tropomyosin α-4 chain, TPM4	46	4	38	5		
Tropomodulin-3, TMOD3	35	0	52	0		
Other cytoskeletal proteins						
Kinesin-like protein KIF14, KIF14	89	0	212	0	Smith *et al.* (2010)	
Tubulin α-4A chain, TUBA4A	25	52	0	0		

TABLE 1: **Most abundant specific interactors with GFP-tagged supervillin and anillin.**

Continues

	Total spectral counts (minus background)					
	M phase		Unsynchronized		Known interactors	
Protein	SVIL	ANLN	SVIL	ANLN	Supervillin	Anillin
Tubulin α-1C chain, TUBA1C	25	74	0	0		
Signaling proteins						
14-3-3 protein epsilon, YWHAE	63	5	69	0	Jin *et al.* (2004)	
14-3-3 protein gamma, YWHAG	31	0	51	0	Jin *et al.* (2004)	
Ras GTPase-activating-like protein IQGAP1	45	9	68	4		
DNA-dependent protein kinase catalytic subunit, PRKDC	31	2	14	0		
Myosin phosphatase Rho-interacting protein, MPRIP	27	0	24	0		
CD2-associated protein, CD2AP	0	56	0	225		Monzo *et al.* (2005)
SH3 domain-containing kinase-binding protein 1, SH3KBP1/CIN85/Cindr	0	25	0	157		Haglund *et al.* (2010)
Ser/Thr-protein phosphatase 2A regulatory subunit A α, PPP2R1A	6	20	14	21		
Ser/Thr-protein phosphatase 2A regulatory subunit B α, PPP2R2A	6	20	13	18		
(Citron Rho-interacting kinase, CIT/CTRO)	*0*	*13*	*0*	*0*		Gai *et al.* (2011)
Other Proteins						
Nucleophosmin, NPM1	13	20	7	3		
Nucleolin, NCL	5	22	0	0		
60S ribosomal protein L4, RPL4	5	27	0	0		
60S ribosomal protein L7, RPL7	2	20	4	7		

Total specific spectral counts, minus any background counts observed in EGFP-only samples, for the 43 most abundant (of 265 total) proteins that coisolated in triplicate analyses with EGFP-tagged human supervillin (SVIL) or anillin (ANLN) and anti-GFP nanobody affinity beads from M-phase–enriched (M phase) and unsynchronized HeLa cells (unsynchronized). Only proteins represented by >20 specific peptides, e.g., an average of ~7 peptides/experiment, are shown. Citron Rho-interacting kinase, in italics, is included because of its documented interaction with anillin. References cite previously documented interactions.

TABLE 1: **Most abundant specific interactors with GFP-tagged supervillin and anillin. Continued**

promotes Rho-induced activation of linear actin assembly by formins (Higashi *et al.*, 2010), and gelsolin may directly regulate myosin II activity at cell–substrate adhesions through calcium-dependent binding to MHC (Arora *et al.*, 2013). Other supervillin-selective interactors are the signaling proteins IQGAP1, PRKDC, and MPRIP/p116Rip. IQGAP1 is a large multidomain protein that regulates numerous motile processes, including cytokinesis (Shannon, 2012). PRKDC is a large member of the phosphoinoside-3/phosphoinoside-4 kinase family that has been primarily studied for its role in DNA repair and p53-mediated apoptosis after exposure to ionizing radiation but also has been implicated in mitotic progression (Stephan *et al.*, 2009; Hill and Lee, 2010). Although it is not known to regulate cytokinesis, MPRIP recruits myosin phosphatase to unbranched actin filaments and thus regulates pMRLC activation (Koga and Ikebe, 2005; Surks *et al.*, 2005). Conversely, serine/threonine protein phosphatase 2A emerged as a novel candidate interactor for anillin (Table 1); homologues of this protein regulate myosin II assembly or cytokinesis in yeast and soil amoeba (Rai and Egelhoff, 2011; Goyal and Simanis, 2012). Thus, most of the newly identified abundant interactors are known or plausible participants in cytokinetic signaling pathways. The reproducible differences in interaction partners between supervillin and anillin suggest that these proteins participate in distinguishable pathways that overlap to regulate myosin II function at the furrow.

DISCUSSION

We show here that the MHC-binding site within supervillin lies within residues 99–153 and that loss of myosin II binding leads to dominant-negative disruption of cell division and loss of ability to rescue supervillin depletion. Point mutagenesis suggests that at least five regions of local charge are involved in the supervillin–MHC interaction. Supervillin residues 93–125 were previously implicated in binding to myosin II by proteolytic mapping (Chen *et al.*, 2003) and are unstructured although predicted to be capable of ligand-dependent folding (Meszaros *et al.*, 2009; Fedechkin *et al.*, 2013). Supervillin amino acids 1–10 also contribute to binding avidities for both MHC and L-MLCK, although they are not sufficient for binding to either protein. These residues may be part of secondary, lower-avidity interactions for each protein or be important for ligand-dependent structural rearrangements that facilitate tight binding.

We also show here that supervillin binding to myosin II is required for efficient cytokinesis; that this phenotype is similar to, but occurs

somewhat later than, cell division defects caused by loss of anillin from human cells (Straight *et al.*, 2005; Zhao and Fang, 2005); and that supervillin synergizes with anillin to regulate myosin II at the furrow. In supervillin-knockdown cells, some cortical MHC redistributes away from the furrow, beginning in late anaphase, whereas pMRLC distribution is aberrant only in early anaphase and at the bridge stage. Of interest, Rab21-associated integrin trafficking, a process facilitated by supervillin (Fang *et al.*, 2010), is similarly required for both initial myosin activation signaling and membrane recruitment to the ends of the invaginating furrow (Pellinen *et al.*, 2008). Because anillin localizes normally in supervillin-knockdown cells until bridge formation, it is apparently sufficient for myosin II activation at the furrow during late anaphase and telophase. In supervillin-knockdown cells, the overexpression and redistribution of anillin to the bridge ends and the apical cortices of nascent daughter cells, which are characteristic localizations for supervillin (Smith *et al.*, 2010), may allow anillin to partially compensate for supervillin depletion from cytokinetic bridges. Functional cross-talk between supervillin and anillin is further supported by the mislocalization of supervillin in anillin-knockdown cells and the more-than-additive effects observed after double knockdowns of both proteins. Taken together, these results suggest that anillin and supervillin coordinate during the initial activation of myosin II in the anaphase cortex, anillin plays the primary role in myosin activation during later anaphase and telophase, and supervillin is required primarily for cortical constriction or membrane trafficking during bridge elongation or closure.

Proteomic identifications of supervillin and anillin interactors support the presence of separate functional pathways that coordinately regulate cytokinesis. Supervillin and anillin apparently do not interact directly, but each binds to both MHC and F-actin. Not all reported binding partners were identified in the affinity isolates, possibly due to insolubility of very large complexes or the loss of proteins with lower avidities. Nonetheless, many interactors with signaling capabilities show specificity for one protein or the other. These results suggest overlap of function between supervillin and anillin at the level of myosin II recruitment and activation, with each protein playing a key role at the cortex at different stages of cell division. The greater association of actin-binding proteins with supervillin, especially the abundance of stress fiber–associated proteins, is reminiscent of observations in *Drosophila* cells, in which unbranched actin filaments are required for continued myosin II localization at the furrow (Dean *et al.*, 2005). The number of supervillin-associated unconventional myosins raises questions about whether their motor or actin-binding activities contribute to membrane trafficking or cortical tension during the later stages of bridge narrowing.

The interactions of supervillin and anillin with different central spindle and signaling proteins suggest that each can promote scaffolding or signaling between the furrow cortex and the central spindle (Figure 5A). Furthermore, the second region of supervillin important for normal cell division (SV-831–1281) contains the KIF14-interaction site (Smith *et al.*, 2010) and potentially a binding site for PRC1 (Hasegawa *et al.*, 2013), both of which are required for central spindle assembly (Carleton *et al.*, 2006; Neef *et al.*, 2007; Shrestha *et al.*, 2012). The interaction of KIF14 with citron kinase (Gruneberg *et al.*, 2006; Watanabe *et al.*, 2013), which coisolates with anillin (Table 1; Gai *et al.*, 2011), suggests that supervillin and anillin could each link the cortex with separate-but-interacting components of the central spindle.

While this work was in revision, another report also proposed supervillin as a molecular link between myosin II activation and central spindle function (Hasegawa *et al.*, 2013). These researchers showed that supervillin epitopes are found at the central spindle under fixation conditions that reduce the cortical signal and that supervillin residues 676–1009 bind directly to PRC1. In addition, cleavage furrows became elongated in the absence of the MHC/L-MLCK–interacting supervillin N-terminus or after mutation to alanine of Ser-238, a residue that is phosphorylated by polo-like kinase 1 (PLK1), a PRC1-binding partner and cytokinesis regulator (Hu *et al.*, 2012). These supervillin mutations reduced pMRLC localization at the furrow during ingression (Hasegawa *et al.*, 2013). These results are consistent with our observations that the loss of supervillin decreases the proportion of total MHC at the furrow during anaphase II and telophase and affects the proportion of furrow pMRLC during early anaphase and bridge formation. The results of Hasegawa *et al.* (2013) also may explain the failure of bSV, which naturally has an alanine at position 238, to substitute for human supervillin in rescue experiments and imply that not all functional regulatory sites in the supervillin N-terminus are conserved across species.

Supervillin is likely to be differentially important for cytokinesis in vertebrate cells, as opposed to other organisms. First, although a sequence 70% identical (85% similar) to the MHC-binding site in human supervillin is found in sea urchin supervillin (XP_784024.3), no sequences similar to those implicated in L-MLCK binding (residues 1–10 and 23–101) are present. This suggests a different regulatory mechanism in sea urchin, the only organism in which MLCK is known to play a major role in activating myosin II during cell division (Lucero *et al.*, 2006; Uehara *et al.*, 2008). Second, the MHC- and L-MLCK–binding N-terminal sequences identified here are absent from fly and worm supervillin homologues (CG33232; viln-1/C10H11.1), potentially explaining why anillin knockdown in *Drosophila* Kc167 cells displays more penetrance than is observed in HeLa cells (Straight *et al.*, 2005). Taken together, these observations suggest that supervillin may act as a genetic buffer for anillin function to ensure the fidelity of cytokinetic bridge formation and midbody formation in vertebrates.

We conclude that the myosin II–binding capability of supervillin is required for high-fidelity cell division and that supervillin helps to recruit and activate myosin II in the furrow cortex, especially during the bridge stage of cytokinesis. The identities of supervillin and anillin interactors suggest that each may scaffold the central spindle with the furrow cortex, with supervillin associating with myosin II, unbranched actin filaments, and signaling proteins, many of which play important roles in interphase processes, including cell migration and membrane trafficking. Thus, during both interphase and cytokinesis, supervillin integrates dynamic processes involving membrane signaling cascades, vesicle trafficking, microtubule-rich structures, and the actin- and myosin II–associated membrane cortex.

MATERIALS AND METHODS

Cell culture

Adherent HeLa S3 Tet-Off (Clontech, Mountain View, CA) and COS7 cells were grown as described previously (Smith *et al.*, 2010). HeLa S3 Tet-Off cells stably expressing a GFP fusion to human supervillin, nonmuscle isoform 1 (Fang and Luna, 2013), latently discovered to bear a point mutation (K923E), were cultured in the HeLa medium. All experiments were performed in six-well culture dishes containing 22-mm^2 coverslips, except for production of extracts used in GST pull downs and GFP nanobody affinity isolations (see later descriptions). All cultures were grown at 37°C in 5% CO_2.

Antibodies

For immunoblotting, rabbit anti-supervillin (H340; Nebl *et al.*, 2002; Oh *et al.*, 2003) was used at 1:1000. Rabbit antibody against amino acids 417–687 in human anillin was a kind gift from Michael Glotzer

(University of Chicago; Piekny and Glotzer, 2008) and used at 1:5000. Mouse monoclonal anti-actin (C4; Millipore, Temecula, CA) was used at 1:3000. Rabbit monoclonal anti-GFP (D5.1; Cell Signaling, Beverly, MA) was used at 1:1000. Rabbit polyclonal anti–myosin IIA (Covance, Princeton NJ) was used at 1:10,000. Horseradish peroxidase–conjugated donkey anti-mouse and anti-rabbit antibodies (Jackson ImmunoResearch, West Grove, PA) were used at 1:20,000.

For immunofluorescence, HeLa cells were stained with mouse monoclonal anti-pMRLC (Ser-19; 1:200; Cell Signaling), rabbit anti-anillin (1:1500), or rabbit polyclonal anti–myosin IIA (1:200; Covance). COS7 cells were stained with rabbit polyclonal anti-myosin IIB (1:100; Covance). Rabbit polyclonal anti-EGFP (1:1000; Abcam, Cambridge, MA) was used to enhance the EGFP-supervillin signal in the stable HeLa cell line (Smith *et al.*, 2010). Secondary antibodies were goat anti-rabbit or anti-mouse Alexa Fluor 488 conjugates (HeLa) and goat anti-rabbit Alexa Fluor 568 (COS7; Life Technologies, Grand Island, NY). Actin and DNA were visualized using Alexa Fluor 568–phalloidin (Life Technologies) and Hoechst, respectively.

RNA interference

Stealth (Life Technologies) duplex sequence for SV-6016-6040 (SVKD-2) was described previously (Smith *et al.*, 2010); this dsRNA targets a 3′-UTR sequence absent from EGFP-supervillin. The following Stealth dsRNA sequences also were used: 5′-GAACUAUGAAGGACCACCAGAGAUA (scrambled control) and 5′-GAAGAUAUCGAAGCCAGACCAGAUA against a coding sequence present in both endogenous and EGFP-tagged human supervillin (SVKD-1;SV-2473-2497).5′-ACGAAAGGGUUUGUGCCAAUAUUCA (AnilKD-1; ANLN-3473-3497) and 5′-CGUGAUAUGACUUGUUACUAGGGUA (AnilKD-2; ANLN-3800-3824) were used to knock down anillin.

Plasmids

The nonmuscle myosin IIA-S2 region was subcloned from 6xHis-NMIIAS2 vector, a kind gift from Mitsuo Ikebe (University of Massachusetts Medical School), and transferred into pGEX-6P-3 (GE Healthcare Life Sciences, Piscataway, NJ) by restriction digest using *Eco*RI and *Xho*I (New England Biolabs, Beverly, MA). A vector encoding a GST fusion with the six Ig domains of the L-MLCK N-terminus, amino acids 2–867 (L-MLCK-6Ig), was a kind gift from Anne Bresnick (Albert Einstein College of Medicine; Dulyaninova *et al.*, 2004). EGFP-hSV was generated by PCR (Pope *et al.*, 1998) and ligated into pEGFP-C2 between *Eco*RI and *Xba*I in two steps by Zhiyou Fang (University of Massachusetts Medical School; Fang and Luna, 2013). First, a 3′ *Eco*RV/*Xba*I fragment was ligated into pEGFP-C2 digested with *Sma*I and *Xba*I. This vector was then digested with *Eco*RI and ligated with an *Eco*RI fragment containing the hSV 5′ sequence. EGFP (Clontech), EGFP-bSV, bSV-1–171-EGFP, EGFP-bSV-171–1792, EGFP-bSV-1–830, EGFP-bSV-831–1281, EGFP-bSV-1–1009, EGFP-bSV-1010–1792, EGFP-bSV-831–1792, EGFP-bSV-1–342, and bSV-1–174-EGFP were described previously (Wulfkuhle *et al.*, 1999; Chen *et al.*, 2003; Takizawa *et al.*, 2007). EGFP-bSV-1–174 was created by converting residue G175 in EGFP-bSV1–342 (Wulfkuhle *et al.*, 1999) to a stop codon using the QuikChange Site-Directed Mutagenesis kit (Agilent Technologies, Santa Clara, CA). Two C-terminal deletion constructs were made by restriction digestion of EGFP-bSV-1–342. Digestion with *Bam*HI (New England Biolabs) and religation resulted in EGFP-bSV-1–127; digestion with *Xho*I (New England Biolabs) and religation produced EGFP-bSV-1–101. EGFP-bSV-1–23 was created by converting residue L24 to a stop codon. EGFP-bSV-11–174 and bSV-11–174-EGFP were created by PCR using EGFP-bSV-1–830 as template. The resulting fragments were then ligated in-frame into either the pEGFP-C1 or -N3 vector (Clontech). EGFP-bSV-72–174 and bSV-93–174-EGFP were created by converting residues R72 and S73 in bSV-1–174 to a *Bgl*II restriction site, followed by digestion with *Bgl*II (New England Biolabs) and religation. All primers for point mutagenesis and PCR are listed in Supplemental Table S1.

Targeted alanine mutations were introduced into bSV-1–174 and hSV-1–330 using the QuikChange kit as described and primers listed in Supplemental Table S1. To mutate a total of four residues in bSV-1–11 and bSV-33–51, a second set of primers was used to introduce additional mutations into bSV-1–174-R9A,R10A and bSV-1–174-M43A,R44A. EGFP-bSV-1–174 mutants were restriction digested with *Nhe*I and *Pvu*I (New England Biolabs) and cloned into the corresponding restriction sites in EGFP-bSV-1–1792. EGFP-hSV-1–330 mutants were restriction digested with *Nhe*I-HF and *Bst*EII-HF (New England Biolabs) and ligated into the corresponding sites in EGFP-hSV-1–1788. All constructs and mutations were verified by sequencing.

Transfections and protein extractions

For protein knockdowns, HeLa cells were reverse transfected with 20 nM total dsRNA (20 nM control, or 10 nM each of control and either supervillin or anillin dsRNAs) and 5 µl of Lipofectamine RNAiMAX (Life Technologies), according to the manufacturer's instructions. In rescue experiments, 4 µl of Lipofectamine 2000 (Life Technologies) was used to reverse transfect dsRNAs (20 nM total concentration) and plasmid DNA (1.5–4.0 µg) together, and cells were grown on coverslips coated with bovine fibronectin (Sigma-Aldrich, St. Louis, MO; Smith *et al.*, 2010). After transfection, cells were incubated for 48 h before fixation with 4% paraformaldehyde or extraction with RIPA buffer containing protease inhibitors (Smith *et al.*, 2010). To produce extracts for GST pull-down experiments, HeLa cells were plated in 6-cm dishes and incubated overnight before transfection using Lipofectamine 2000 and either EGFP or EGFP-tagged BSV-1–174 deletion and mutation constructs. After 24 h of expression, cells were extracted with RIPA buffer lacking SDS and clarified by centrifugation at 16,000 × *g* for 15 min at 4°C (Smith *et al.*, 2010). Each 6-cm dish extract was divided for use in pull downs with both GST–myo-S2 and GST–L-MLCK-6Ig.

For visualization of proteins during cell division, cells were synchronized at the G2/M transition by incubation for 20 h with 10 µM RO-3306 (Enzo Life Sciences, Farmingdale, NY), a reversible Cdk1 inhibitor (Vassilev, 2006). Cells were released by rinsing three times with D-PBS (Life Technologies) and then incubated at 37°C with fresh medium for 90–105 min before fixation in 4% paraformaldehyde and staining. To screen for dominant-negative effects of EGFP-bSV proteins on cell division, cells were reverse transfected as described, incubated overnight, synchronized with RO-3306, and then released for 4–18 h before fixation and staining.

COS7 cells were seeded on coverslips for 24 h before being transfected with 1–1.5 µg of EGFP-tagged constructs and 10 µl Effectene transfection reagent (Qiagen, Valencia, CA). Cells were then incubated for 24 h before fixation with 4% paraformaldehyde and staining.

Imaging and equatorial:polar ratio determination

Cells were imaged using an Axioskop fluorescence microscope with Plan-NeoFluor objectives (Carl Zeiss Microscopy, Thornwood, NY), as described previously (Smith *et al.*, 2010). Protein localizations in dividing HeLa cells and myosin II punctae in COS7 cells were imaged using a 100× (numerical aperture [NA] 1.3) oil immersion

objective. Numbers of binucleated/multinucleated HeLa cells were assayed using a 40× (NA 0.9) objective lens, and representative overviews for Figure 5B were obtained with a 25× (NA 0.8) objective. Images were uniformly adjusted for brightness and contrast, and merged images were assembled with Photoshop (Adobe, San Jose, CA).

Average signal intensities at the equatorial and polar cortices were determined using a modification of the method of Robinson *et al.* (2002). The polygon tool in ImageJ (National Institutes of Health, Bethesda, MD) was used to select areas with widths of ~0.4 µm that covered the cortex signal along the regions of the cell indicated in Figures 2 and 7. Mean signal intensities for these boxes were obtained by using the Measure function under the Analyze menu with area, mean signal intensity, and SD selected for output. Measurements were made for each pole and each side of the furrow (Figure 2), which were then averaged using Excel (Microsoft, Redmond, WA) before calculating the ratio of equatorial to polar signal. For anillin localization at the midbody (Figure 7), signal intensities along the daughter cell cortices proximal to the midbody were analyzed and averaged as before, but the midbody signal itself was taken as one measurement. InStat software, version 3 (GraphPad Software, San Diego, CA), was used to calculate means and SD and perform statistical tests.

GST pull down and SDS–PAGE

Fusion proteins were made using Rosetta DE3 pLysS competent *Escherichia coli* (EMD4Biosciences, La Jolla, CA), as previously described (Swaffield and Johnston, 2001; Chen *et al.*, 2003; Smith *et al.*, 2010). GST pull-down assays were performed as previously described (Smith *et al.*, 2010). HeLa cell lysates were separated on 5–15% gradient SDS–PAGE gels and transferred to Protran nitrocellulose (Whatman, Dassel, Germany) to confirm knockdown of supervillin and anillin proteins and expression of EGFP-SV. Extracts containing bSV-1–174 proteins were run on 10% SDS–PAGE gels. Blots were visualized using either Supersignal WestPico or WestFemto ECL reagents (Thermo Scientific, Rockford, IL) on a Kodak Image Station (Eastman Kodak, Rochester, NY). Protein band densities were obtained using Kodak Molecular Imaging Software, version 4.0 (Eastman Kodak) and ratios calculated using Excel.

GFP nanobody affinity isolations

Protein affinity isolations were performed using a GFP nanobody covalently bound to magnetic beads. Isolations were performed in triplicate, with replicates carried out on separate days. HeLa cells from a subconfluent T-75 flask were split into three 10-cm dishes and incubated overnight. Cells were then transfected using Lipofectamine 2000 and 13 µg of EGFP, EGFP-anillin, or EGFP-hSV and incubated for 24 h before extraction. To enrich for dividing cells, plates were incubated for 3 h after transfection and then treated with 10 µM RO-3306 (Enzo Life Sciences), as described. Cells were released from synchronization for 100 min before extraction. Cells were extracted with 1 ml of RIPA buffer with protease inhibitors but lacking SDS (Smith *et al.*, 2010). Ten microliters (per extract) of anti-GFP nanobody-conjugated beads (Domanski *et al.*, 2012) were washed three times in cold RIPA buffer lacking SDS before the addition of 900 µl of cleared lysate. Strong magnets were used at each step to separate the beads from the lysate and washes. After incubation for 1 h at 4°C with rotation, the beads were transferred to a fresh tube and washed three times with ice-cold RIPA buffer lacking SDS. Proteins were eluted from the magnetic beads with 2% SDS and run on either 5–15% acrylamide SDS gels (Laemmli, 1970) for silver staining or 10% SDS–PAGE for in-gel digestion and analysis by liquid chromatography and tandem mass spectrometry (LC-MS/MS).

In-gel digestion

Samples for in-gel digestion were run ~1.5 cm into the resolving area of 10% minigels and stained with a ProteoSilver Silver Stain Kit (Sigma-Aldrich). Protein-containing regions were excised, destained, and cut into 1 × 1 mm pieces. Gel pieces were placed in 1.5-ml microcentrifuge tubes with 1 ml of water for 1 h. The water was removed, and 125 µl/tube 250 mM ammonium bicarbonate was added. Disulfide bonds were reduced by adding 25 µl/tube 45 mM 1,4-dithio-D-threitol and incubating for 30 min at 50°C. Samples were cooled to room temperature and alkylated for 30 min with 25 µl/tube 100 mM iodoacetamide. Gel slices were washed twice with 1-ml aliquots of water and incubated at room temperature for 1 h with 1 ml/tube of a 50:50 mixture of 50 mM ammonium bicarbonate:acetonitrile. This solution was replaced with 200 µl/tube of acetonitrile, at which point the gel slices turned opaque white. After removal of acetonitrile, the gel slices were further dried in a Savant SpeedVac (Thermo Scientific, Asheville, NC). Gel slices were rehydrated in 75 µl/tube of 2 ng/µl trypsin (Sigma-Aldrich) in 0.01% ProteaseMAX Surfactant (Promega, Madison, WI) and 50 mM ammonium bicarbonate. Additional aliquots of 50 mM ammonium bicarbonate were added, as necessary, to fully submerge the gel slices. Samples were incubated for 21 h at 37°C. Supernatants were removed to separate 1.5-ml microcentrifuge tubes. Gel slices were extracted further with 100 µl/tube of 80:20 acetonitrile:1% formic acid. Extracts for each sample were combined, and the tryptic peptides were dried in a SpeedVac.

LC-MS/MS

Dried tryptic peptides were dissolved in 25 µl of 0.1% trifluoroacetic acid and 5% acetonitrile, and a 3-µl aliquot was directly injected onto a custom-packed trap column (2 cm × 100 µm C18). Peptides were eluted and sprayed from a custom-packed emitter (25 cm × 75 µm C18) with a linear gradient from 100% solvent A (0.1% formic acid, 5% acetonitrile) to 35% solvent B (0.1% formic acid, acetonitrile) in 90 min at a flow rate of 300 nl/min on a Proxeon Easy nanoLC system directly coupled to a LTQ Orbitrap Velos mass spectrometer (Thermo Scientific). Data-dependent scans were acquired according to a scheme in which full MS scans from 350 to 2000 *m/z* were acquired in the Orbitrap Velos at a resolution of 60,000, followed by 10 MS/MS scans acquired in the LTQ ion trap instrument. The raw data files were processed with Extract_ MSN (Thermo Scientific) into peak lists and then searched against the Human index of the SwissProt database using the Mascot Search engine, version 2.4 (Matrixsciences, London, United Kingdom). Parent mass tolerances were set to 10 ppm, and fragment mass tolerances were set to 0.5 Da. The variable modifications of acetyl (protein N-terminus), pyro glutamic for N-terminal glutamine, carbamidomethylation of cysteine, and oxidation of methionine were used. Mascot search results were loaded into Scaffold4 software (Proteome Software, Portland, OR) for comparisons of sample results. Cosedimenting proteins were screened using conservative parameters, with a positive identification requiring a protein threshold of 99% and a minimum of two peptides per protein, with a peptide threshold of 95%. The estimated Prophet false discovery rate at these settings is <0.4%.

Proteins present in EGFP-only affinity isolates at spectral count levels ≥50% of the number of peptides identified in EGFP-hSV or EGFP-anillin fractions were defined as contaminants and eliminated; these proteins are listed in Supplemental Table S2. The most abundant interactors are presented in Table 1. All identified proteins

meeting the cut-off parameters and the spectral counts from each experiment, including background counts, are reported in Supplemental Tables S3 and S4.

ACKNOWLEDGMENTS

We thank Mary Thompson, Sarah Keegan, and David Fenyo for generous assistance and support during the design and production of the GFP nanobody beads. We also thank Cheryl L. Gatto for construction of the bSV-1–171-EGFP plasmid, Zhiyou Fang for the EGFP-tagged human supervillin plasmids, Anne Bresnick for the gift of the GST–L-MLCK N-terminus plasmid, and Mitsuo Ikebe for generously providing the histidine-tagged myosin S2 plasmid. We gratefully acknowledge Michael Glotzer for providing anillin antibody and pEGFP-anillin plasmid. In addition, we thank Li-Ting Su of the University of California, San Diego, for alerting us to the presence of the K923E point mutation in the original EGFP-tagged human supervillin construct. We also thank Dannel McCollum for comments on the manuscript and Zhiyou Fang and Kay Son for their advice and experimental suggestions. This work was supported by National Institutes of Health Grants R01 GM033048–26S1 (E.J.L.), U54 GM103511 (B.T.C. and M.P.R.), and P41 GM103314 (B.T.C.) and the Department of Cell and Developmental Biology at the University of Massachusetts Medical School.

REFERENCES

Ahmed SM, Theriault BL, Uppalapati M, Chiu CW, Gallie BL, Sidhu SS, Angers S (2012). KIF14 negatively regulates Rap1a-Radil signaling during breast cancer progression. J Cell Biol 199, 951–967.

Archer SK, Claudianos C, Campbell HD (2005). Evolution of the gelsolin family of actin-binding proteins as novel transcriptional coactivators. Bioessays 27, 388–396.

Arora PD, Wang Y, Bresnick A, Dawson J, Janmey PA, McCulloch CA (2013). Collagen remodeling by phagocytosis is determined by collagen substrate topology and calcium-dependent interactions of gelsolin with nonmuscle myosin IIA in cell adhesions. Mol Biol Cell 24, 734–747.

Avanzi MP, Chen A, He W, Mitchell WB (2012). Optimizing megakaryocyte polyploidization by targeting multiple pathways of cytokinesis. Transfusion 52, 2406–2413.

Bhuwania R, Cornfine S, Fang Z, Kruger M, Luna EJ, Linder S (2012). Supervillin couples myosin-dependent contractility to podosomes and enables their turnover. J Cell Sci 125, 2300–2314.

Carleton M, Mao M, Biery M, Warrener P, Kim S, Buser C, Marshall CG, Fernandes C, Annis J, Linsley PS (2006). RNA interference-mediated silencing of mitotic kinesin KIF14 disrupts cell cycle progression and induces cytokinesis failure. Mol Cell Biol 26, 3853–3863.

Chalamalasetty RB, Hummer S, Nigg EA, Sillje HH (2006). Influence of human Ect2 depletion and overexpression on cleavage furrow formation and abscission. J Cell Sci 119, 3008–3019.

Chen Y, Takizawa N, Crowley JL, Oh SW, Gatto CL, Kambara T, Sato O, Li X, Ikebe M, Luna EJ (2003). F-actin and myosin II binding domains in supervillin. J Biol Chem 278, 46094–46106.

Chircop M, Oakes V, Graham ME, Ma MP, Smith CM, Robinson PJ, Khanna KK (2009). The actin-binding and bundling protein, EPLIN, is required for cytokinesis. Cell Cycle 8, 757–764.

Crowley JL, Smith TC, Fang Z, Takizawa N, Luna EJ (2009). Supervillin reorganizes the actin cytoskeleton and increases invadopodial efficiency. Mol Biol Cell 20, 948–962.

D'Avino PP (2009). How to scaffold the contractile ring for a safe cytokinesis—lessons from anillin-related proteins. J Cell Sci 122, 1071–1079.

Dean SO, Rogers SL, Stuurman N, Vale RD, Spudich JA (2005). Distinct pathways control recruitment and maintenance of myosin II at the cleavage furrow during cytokinesis. Proc Natl Acad Sci USA 102, 13473–13478.

Domanski M, Molloy K, Jiang H, Chait BT, Rout MP, Jensen TH, LaCava J (2012). Improved methodology for the affinity isolation of human protein complexes expressed at near endogenous levels. Biotechniques, doi: 10.2144/000113864.

Dulyaninova NG, Patskovsky YV, Bresnick AR (2004). The N-terminus of the long MLCK induces a disruption in normal spindle morphology and metaphase arrest. J Cell Sci 117, 1481–1493.

Echard A, Hickson GR, Foley E, O'Farrell PH (2004). Terminal cytokinesis events uncovered after an RNAi screen. Curr Biol 14, 1685–1693.

Fang ZY, Luna EJ (2013). Supervillin-mediated suppression of p53 protein enhances cell survival. J Biol Chem 288, 7918–7929.

Fang Z, Takizawa N, Wilson KA, Smith TC, Delprato A, Davidson MW, Lambright DG, Luna EJ (2010). The membrane-associated protein, supervillin, accelerates F-actin-dependent rapid integrin recycling and cell motility. Traffic 11, 782–799.

Fedechkin SO, Brockerman J, Luna EJ, Yu Lobanov M, Galzitskaya OV, Smirnov SL (2013). An N-terminal, 830-residue intrinsically disordered region of the cytoskeleton-regulatory protein supervillin contains myosin II- and F-actin-binding sites. J Biomol Struct Dyn 31, 1150–1159.

Field CM, Alberts BM (1995). Anillin, a contractile ring protein that cycles from the nucleus to the cell cortex. J Cell Biol 131, 165–178.

Freeman AK, Morrison DK (2011). 14-3-3 Proteins: diverse functions in cell proliferation and cancer progression. Semin Cell Dev Biol 22, 681–687.

Frenette P, Haines E, Loloyan M, Kinal M, Pakarian P, Piekny A (2012). An anillin-Ect2 complex stabilizes central spindle microtubules at the cortex during cytokinesis. PLoS One 7, e34888.

Gai M, Camera P, Dema A, Bianchi F, Berto G, Scarpa E, Germena G, Di Cunto F (2011). Citron kinase controls abscission through RhoA and anillin. Mol Biol Cell 22, 3768–3778.

Goyal A, Simanis V (2012). Characterization of ypa1 and ypa2, the *Schizosaccharomyces pombe* orthologs of the peptidyl proyl isomerases that activate PP2A, reveals a role for Ypa2p in the regulation of cytokinesis. Genetics 190, 1235–1250.

Green RA, Paluch E, Oegema K (2012). Cytokinesis in animal cells. Annu Rev Cell Dev Biol 28, 29–58.

Gruneberg U, Neef R, Li X, Chan EH, Chalamalasetty RB, Nigg EA, Barr FA (2006). KIF14 and citron kinase act together to promote efficient cytokinesis. J Cell Biol 172, 363–372.

Haglund K, Nezis IP, Lemus D, Grabbe C, Wesche J, Liestol K, Dikic I, Palmer R, Stenmark H (2010). Cindr interacts with anillin to control cytokinesis in *Drosophila melanogaster*. Curr Biol 20, 944–950.

Han MY, Kosako H, Watanabe T, Hattori S (2007). Extracellular signal-regulated kinase/mitogen-activated protein kinase regulates actin organization and cell motility by phosphorylating the actin cross-linking protein EPLIN. Mol Cell Biol 27, 8190–8204.

Hasegawa H, Hyodo T, Asano E, Ito S, Maeda M, Kuribayashi H, Natsume A, Wakabayashi T, Hamaguchi M, Senga T (2013). Role of SVIL phosphorylation by PLK1 in myosin II activation and cytokinetic furrowing. J Cell Sci 126, 3627–3637.

Havrylov S, Ichioka F, Powell K, Borthwick EB, Baranska J, Maki M, Buchman VL (2008). Adaptor protein Ruk/CIN85 is associated with a subset of COPI-coated membranes of the Golgi complex. Traffic 9, 798–812.

Hickson GR, O'Farrell PH (2008). Rho-dependent control of anillin behavior during cytokinesis. J Cell Biol 180, 285–294.

Higashi T, Ikeda T, Murakami T, Shirakawa R, Kawato M, Okawa K, Furuse M, Kimura T, Kita T, Horiuchi H (2010). Flightless-I (Fli-I) regulates the actin assembly activity of diaphanous-related formins (DRFs) Daam1 and mDia1 in cooperation with active Rho GTPase. J Biol Chem 285, 16231–16238.

Hill R, Lee PW (2010). The DNA-dependent protein kinase (DNA-PK): more than just a case of making ends meet? Cell Cycle 9, 3460–3469.

Hu CK, Ozlu N, Coughlin M, Steen JJ, Mitchison TJ (2012). Plk1 negatively regulates PRC1 to prevent premature midzone formation before cytokinesis. Mol Biol Cell 23, 2702–2711.

Jin J *et al.* (2004). Proteomic, functional, domain-based analysis of in vivo 14-3-3 binding proteins involved in cytoskeletal regulation and cellular organization. Curr Biol 14, 1436–1450.

Johnson RI, Seppa MJ, Cagan RL (2008). The *Drosophila* CD2AP/CIN85 orthologue Cindr regulates junctions and cytoskeleton dynamics during tissue patterning. J Cell Biol 180, 1191–1204.

Knecht DA, Loomis WF (1987). Antisense RNA inactivation of myosin heavy chain gene expression in *Dictyostelium discoideum*. Science 236, 1081–1086.

Koga Y, Ikebe M (2005). p116Rip decreases myosin II phosphorylation by activating myosin light chain phosphatase and by inactivating RhoA. J Biol Chem 280, 4983–4991.

Laemmli UK (1970). Cleavage of structural proteins during the assembly of the head of bacteriophage T4. Nature 227, 680–685.

Li M, Brooks CL, Kon N, Gu W (2004). A dynamic role of HAUSP in the p53-Mdm2 pathway. Mol Cell 13, 879–886.

Lucero A, Stack C, Bresnick AR, Shuster CB (2006). A global, myosin light chain kinase-dependent increase in myosin II contractility accompanies the metaphase-anaphase transition in sea urchin eggs. Mol Biol Cell 17, 4093–4104.

Maddox AS, Habermann B, Desai A, Oegema K (2005). Distinct roles for two *C. elegans* anillins in the gonad and early embryo. Development 132, 2837–2848.
Matsumura F, Ono S, Yamakita Y, Totsukawa G, Yamashiro S (1998). Specific localization of serine 19 phosphorylated myosin II during cell locomotion and mitosis of cultured cells. J Cell Biol 140, 119–129.
Maupin P, Phillips CL, Adelstein RS, Pollard TD (1994). Differential localization of myosin-II isozymes in human cultured cells and blood cells. J Cell Sci 107(Pt 11), 3077–3090.
Meszaros B, Simon I, Dosztanyi Z (2009). Prediction of protein binding regions in disordered proteins. PLoS Comput Biol 5, e1000376.
Monzo P, Gauthier NC, Keslair F, Loubat A, Field CM, Le Marchand-Brustel Y, Cormont M (2005). Clues to CD2-associated protein involvement in cytokinesis. Mol Biol Cell 16, 2891–2902.
Nebl T, Pestonjamasp KN, Leszyk JD, Crowley JL, Oh SW, Luna EJ (2002). Proteomic analysis of a detergent-resistant membrane skeleton from neutrophil plasma membranes. J Biol Chem 277, 43399–43409.
Neef R, Gruneberg U, Kopajtich R, Li X, Nigg EA, Sillje H, Barr FA (2007). Choice of Plk1 docking partners during mitosis and cytokinesis is controlled by the activation state of Cdk1. Nat Cell Biol 9, 436–444.
Oegema K, Savoian MS, Mitchison TJ, Field CM (2000). Functional analysis of a human homologue of the *Drosophila* actin binding protein anillin suggests a role in cytokinesis. J Cell Biol 150, 539–552.
Oh SW, Pope RK, Smith KP, Crowley JL, Nebl T, Lawrence JB, Luna EJ (2003). Archvillin, a muscle-specific isoform of supervillin, is an early expressed component of the costameric membrane skeleton. J Cell Sci 116, 2261–2275.
Pellinen T *et al*. (2008). Integrin trafficking regulated by Rab21 is necessary for cytokinesis. Dev Cell 15, 371–385.
Pestonjamasp KN, Pope RK, Wulfkuhle JD, Luna EJ (1997). Supervillin (p205): A novel membrane-associated, F-actin-binding protein in the villin/gelsolin superfamily. J Cell Biol 139, 1255–1269.
Piekny AJ, Glotzer M (2008). Anillin is a scaffold protein that links RhoA, actin, myosin during cytokinesis. Curr Biol 18, 30–36.
Poirier CC, Ng WP, Robinson DN, Iglesias PA (2012). Deconvolution of the cellular force-generating subsystems that govern cytokinesis furrow ingression. PLoS Comput Biol 8, e1002467.
Pope RK, Pestonjamasp KN, Smith KP, Wulfkuhle JD, Strassel CP, Lawrence JB, Luna EJ (1998). Cloning, characterization, and chromosomal localization of human supervillin (SVIL). Genomics 52, 342–351.
Poperechnaya A, Varlamova O, Lin PJ, Stull JT, Bresnick AR (2000). Localization and activity of myosin light chain kinase isoforms during the cell cycle. J Cell Biol 151, 697–708.
Rai V, Egelhoff TT (2011). Role of B regulatory subunits of protein phosphatase type 2A in myosin II assembly control in *Dictyostelium discoideum*. Eukaryotic Cell 10, 604–610.
Robinson DN, Cavet G, Warrick HM, Spudich JA (2002). Quantitation of the distribution and flux of myosin-II during cytokinesis. BMC Cell Biol 3, 4.
Salbreux G, Charras G, Paluch E (2012). Actin cortex mechanics and cellular morphogenesis. Trends Cell Biol 22, 536–545.
Samoylenko A *et al*. (2012). Increased levels of the HER1 adaptor protein Rukl/CIN85 contribute to breast cancer malignancy. Carcinogenesis 33, 1976–1984.
Schiel JA, Prekeris R (2013). Membrane dynamics during cytokinesis. Curr Opin Cell Biol 25, 92–98.
Shannon KB (2012). IQGAP family members in yeast, *Dictyostelium*, and mammalian cells. Int J Cell Biol 2012, 894817.
Shrestha S, Wilmeth LJ, Eyer J, Shuster CB (2012). PRC1 controls spindle polarization and recruitment of cytokinetic factors during monopolar cytokinesis. Mol Biol Cell 23, 1196–1207.
Smith TC, Fang Z, Luna EJ (2010). Novel interactors and a role for supervillin in early cytokinesis. Cytoskeleton (Hoboken) 67, 346–364.
Somlyo AV, Wang H, Choudhury N, Khromov AS, Majesky M, Owens GK, Somlyo AP (2004). Myosin light chain kinase knockout. J Muscle Res Cell Motil 25, 241–242.
Stephan H, Concannon C, Kremmer E, Carty MP, Nasheuer HP (2009). Ionizing radiation-dependent and independent phosphorylation of the 32-kDa subunit of replication protein A during mitosis. Nucleic Acids Res 37, 6028–6041.
Straight AF, Field CM, Mitchison TJ (2005). Anillin binds nonmuscle myosin II and regulates the contractile ring. Mol Biol Cell 16, 193–201.
Surks HK, Riddick N, Ohtani K (2005). M-RIP targets myosin phosphatase to stress fibers to regulate myosin light chain phosphorylation in vascular smooth muscle cells. J Biol Chem 280, 42543–42551.
Swaffield JC, Johnston SA (2001). Affinity purification of proteins binding to GST fusion proteins. Curr Protoc Mol Biol Chapter 20, Unit 20.22.
Takizawa N, Ikebe R, Ikebe M, Luna EJ (2007). Supervillin slows cell spreading by facilitating myosin II activation at the cell periphery. J Cell Sci 120, 3792–3803.
Uehara R, Hosoya H, Mabuchi I (2008). In vivo phosphorylation of regulatory light chain of myosin II in sea urchin eggs and its role in controlling myosin localization and function during cytokinesis. Cell Motil Cytoskeleton 65, 100–115.
Vardar D, Chishti AH, Frank BS, Luna EJ, Noegel AA, Oh SW, Schleicher M, McKnight CJ (2002). Villin-type headpiece domains show a wide range of F-actin-binding affinities. Cell Motil Cytoskeleton 52, 9–21.
Vassilev LT (2006). Cell cycle synchronization at the G2/M phase border by reversible inhibition of CDK1. Cell Cycle 5, 2555–2556.
Wang YL (2005). The mechanism of cortical ingression during early cytokinesis: thinking beyond the contractile ring hypothesis. Trends Cell Biol 15, 581–588.
Watanabe S, De Zan T, Ishizaki T, Narumiya S (2013). Citron kinase mediates transition from constriction to abscission through its coiled-coil domain. J Cell Sci 126, 1773–1784.
Werner M, Munro E, Glotzer M (2007). Astral signals spatially bias cortical myosin recruitment to break symmetry and promote cytokinesis. Curr Biol 17, 1286–1297.
Wulfkuhle JD, Donina IE, Stark NH, Pope RK, Pestonjamasp KN, Niswonger ML, Luna EJ (1999). Domain analysis of supervillin, an F-actin bundling plasma membrane protein with functional nuclear localization signals. J Cell Sci 112, 2125–2136.
Zhao WM, Fang G (2005). Anillin is a substrate of anaphase-promoting complex/cyclosome (APC/C) that controls spatial contractility of myosin during late cytokinesis. J Biol Chem 280, 33516–33524.
Zhou Q *et al*. (2010). 14-3-3 coordinates microtubules, Rac, myosin II to control cell mechanics and cytokinesis. Curr Biol 20, 1881–1889.
Zhu C, Zhao J, Bibikova M, Leverson JD, Bossy-Wetzel E, Fan JB, Abraham RT, Jiang W (2005). Functional analysis of human microtubule-based motor proteins, the kinesins and dyneins, in mitosis/cytokinesis using RNA interference. Mol Biol Cell 16, 3187–3199.

Supplemental Materials

Molecular Biology of the Cell

Smith et al.

SUPPLEMENTARY MATERIAL

Supplemental Table S1 (PDF). Primers used for PCR and point mutagenesis. Construct names are in the first column; sense and anti-sense primers are in columns 2 and 3, respectively. Underlined bases indicate imbedded restriction sites used for cloning. Italics indicate mutated bases. The asterisk (*) denotes that this primer pair was used in a second round of mutagenesis with either bSV-R9A,R10A or bSV-M43A,R44A as a template.

Supplemental Table S2 (PDF). Proteins eliminated as contaminants in co-isolates with GFP nanobodies attached to magnetic beads. These proteins were present in EGFP-only affinity isolates at spectral count levels ≥ 50% of the number of peptides identified in EGFP-hSV or EGFP-anillin fractions.

Supplemental Table S3 (MS Excel). All proteins identified in triplicate GFP nanobody affinity isolates using lysates from M-Phase enriched HeLa cells expressing EGFP, EGFP-hSV, or EGFP-anillin. Total spectral counts of identified peptides shown for each replicate. Positive identifications were made as described in the legend for Table 1.

Supplemental Table S4 (MS Excel). All proteins identified in triplicate GFP nanobody affinity isolates using lysates from unsynchronized HeLa cells expressing EGFP, EGFP-hSV, or EGFP-anillin. Positive identifications were made as described in the legend for Table 1.

Supplemental Figure S1. Representative micrographs of interphase cells reported in Figure 1G. Cells were transfected with the indicated EGFP-tagged bovine supervillin constructs for 48 h and evaluated for bi/multinucleate phenotype. Phase images (a, d, g, j, m, p, s, v, y), EGFP (b, e, h, k, n, q, t, w, z), and DNA (c, f, i, l, o, r, u, x, aa). Nuclei of cells expressing EGFP-tagged proteins are indicated with white arrowheads (c, f, i, l, o, r, u, x, aa). Bar = 20 μm.

Supplemental Figure S2. Representative localizations of EGFP-tagged supervillin deletion constructs in dividing cells. EGFP (a-d), bSV-1-171-EGFP (e-h), EGFP-bSV-171-1792 (i-l), EGFP-bSV-1-830 (m-p), EGFP-bSV-1-1009 (q-t), EGFP-bSV-1010-1792 (u-x), and EGFP-bSV-831 - 1281 (y-b'). EGFP (green in merges) shown in a, e, i, m, q, u, and y. Actin (red in merges) shown in b, f, j, n, r, v, and z. DNA (blue in merges), c, g, k, o, s, w, and a'. Merged images in d, h, l, p, t, x, and b'. Phase images in d', h', l', p', t', x', b". Bar = 10 μm.

Supplemental Figure S3. Representative micrographs showing the effects of deletion mutations within bSV-1-174-EGFP on the ability of this protein to form myosin II punctae after overexpression in COS7 cells. EGFP-tagged full-length bSV-1-174 causes hyperactivation of co-localizing myosin II filaments into stable punctae with L-MLCK (Chen *et al.*, 2003; Takizawa *et al.*, 2007). Transfected COS7 cells were stained for myosin IIB heavy chain (MHC-IIB; a, d, g, j, m, p, s, v, y; red in merges) and evaluated for myosin II punctae, indicated at right by (+) punctae formed, (+/-) incomplete conversion, or (-) no punctae. EGFP constructs (b, e, h, k, n, q, t, w, z; green in merges) are: (b) EGFP alone, (e) bSV-1-174-EGFP, (h) EGFP-bSV-1-174, (k) EGFP-bSV-1-127, (n) EGFP-bSV-1-101, (q) EGFP-bSV-1-23, (t) bSV-11-174-EGFP, (w) EGFP-bSV-72-174, and (z) bSV-93-174-EGFP. Merged images (c, f, i, l, o, r, u, x, a'). Bar, 20 μm.

Supplemental Figure S4. Representative micrographs showing the effects of point mutations within bSV-1-174-EGFP on the ability of this protein to form hyperactivated myosin II punctae after overexpression in COS7 cells. Transfected COS7 cells were stained for myosin II heavy chain (a, d, g, j, m, p, s, v, y; red in merges) and evaluated for myosin II-punctae, indicated at right by (+) punctae formed, (+/-) incomplete conversion, and (-) no punctae. EGFP constructs (b, e, h, k, n, q, t, w, z; green in merges) are: (b) bSV-1-174-K4A,R6A,R9A,R10A-EGFP; (e) bSV-1-174-R9A,R10A-EGFP; (h) bSV-1-174-E36A,E37A-EGFP; (k) bSV-1-174-R41A,Y42A-EGFP; (n) bSV-1-174-M43A,R44A-EGFP; (q) bSV-1-174-R107A,Y108A-EGFP; (t)

bSV-1-174-R112A,R113A-EGFP; (w) BSV-1-174-EGFP-E127A,D129A; (z), BSV-1-174-EGFP-R140A,K141A. Merged images (c, f, i, l, o, r, u, x, a'). Bar, 20 μm.

Supplemental Figure S5. Identification of supervillin sequences required for L-MLCK interaction. (A, B, C, D) Bound and unbound deletion and point mutants of EGFP-tagged bSV 1-174, as indicated, in pulldown experiments with the GST-tagged L-MLCK N-terminus. Blots were probed with anti-GFP; Ponceau staining of blots with bound proteins shows equal loading of the GST-tagged bait protein. Ratios of bound:unbound EGFP signal, normalized to 1-174-EGFP ratio, are shown. Ratios ≤ 0.5 were considered to indicate reduction in binding to L-MLCK. $N \geq 2$. (E) Immunoblot of bound and unbound fractions probed for MHC-IIA in cell lysates. Input lysate (lane 1), EGFP (lane 2), bSV-1-174-EGFP (lane 3), bSV-1-174-K4A,R6A,R9A,R10A-EGFP (lane 4), bSV-1-174-R9A,R10A-EGFP (lane 5). Bound and unbound samples were probed on the same blot; Ponceau staining shows GST-L-MLCK-6Ig in bound fractions to verify loading.

	Primers	
Construct	**Sense**	**Antisense**
EGFP-bSV-1-174	5'- GGACTGAGCTCTCG*TA*GCTCAGGACCTGCGT	5'- ACGCAGGTCCTGAG*CTAC*GAGAGCTCAGTCC
EGFP-bSV-1-23	5'- GCCCATCCTCTTG*T*AGAGCTGCACGGG	5'- CCCGTGCAGCTCT*A*CAAGAGGATGGGC
bSV-11-174	5'- CCAGATCTTTAGAAGGAATTGAAACCGACACGCA	5'- GGAATTCAGGCCCGAGAGCTCAGTCCT
bSV-R9A,R10A	5' - GAAAGAATTGC*GC*G*GC*CTTAGAAGGAATTG	5' - CAATTCCTTCTAAG*GC*C*GC*GGCAATTCTTTC
bSV-E36A,E37A	5' - TCGCCTGCTGG*C*GG*C*GGACACACCC	5' - GGGTGTGTCC*G*CC*GC*CAGCAGGCGA
bSV-R41A,Y42A	5' - GGACACACCC*GC*A*GC*CATGCGTGCC	5' - GGCACGCATG*GC*T*GC*GGGTGTGTCC
bSV-M43A,R44A	5' - CACCCAGATA*GC*G*GC*TGCCACAGACC	5' - GGTCTGTGGCA*GC*C*GC*GTATCTGGGTG
bSV-R107A,Y108A	5'- CGAAAGAATCGCC*GC*G*GC*CAAAGCAGAGAGAAG	5'- CTTCTCTCTGCTTTG*GC*C*GC*GGCGATTCTTTCG
bSV-R112A,R113A	5'- TACAAAGCAGAG*GC*A*GC*ACGGCAGCTGG	5'- CCAGCTGCCGT*GC*T*GC*CTCTGCTTTGTA
bSV-E127A,D129A	5'- TGGATCCGG*C*AGCAG*C*CTCTGAAA	5'- TTTCAGAG*GC*TGCT*GC*CGGATCCA
bSV-R140A,K141A	5'- AGCAGGTCC*GC*A*GC*GGACCCCGA	5'- TCGGGGTC*GC*T*GC*GGACCTGCT
***bSV-K4A,R6A,R9A,R10A**	5'- ATGAAAAGA*GC*AGAA*GC*AATTGCCGCGG	5'- CCGCGGCAATT*GC*TTCT*GC*TCCTTTTCAT
***bSV-R41A,Y42A,M43A,R44A**	5'- GGACACACCC*GC*A*GC*CGCGGCTGCC	5'- GGCAGCCGCG*GC*T*GC*GGGTGTGTCC
EGFP-hSV-R140A,K141A	5'- CTATACCAAGTC*GC*G*GC*GGAGCCTGATG	5'- CATCAGGCTCC*GC*C*GC*GGACTTGGTATAG
EGFP-hSV K148A,R149A	5'- ATGCTGTCGAG*GC*G*GC*GGGAGGAAAA	5'- TTTTCCTCCC*GC*C*GC*CTCGACAGCAT

Supplemental Table S1 (PDF). Primers used for PCR and point mutagenesis. Construct names are in the first column; sense and anti-sense primers are in columns 2 and 3, respectively. Underlined bases indicate imbedded restriction sites used for cloning. Italics indicate mutated bases. The asterisk (*) denotes that this primer pair was used in a second round of mutagenesis with either bSV-R9A,R10A or bSV-M43A,R44A as a template.

Supplemental Table S2. Proteins Assigned as Contaminants

	Background Proteins Enriched in EGFP only Samples (98/409)			Total Spectral Counts (M phase)		
		Accession Number	Mol Wt	GFP-ANLN	GFP-hSV	EGFP
Skin Proteins	Keratin, type I cytoskeletal 9 OS=Homo sapiens GN=KRT9 PE=1 SV=3	K1C9_HUMAN	62 kDa	522	844	576
	Keratin, type I cytoskeletal 10 OS=Homo sapiens GN=KRT10 PE=1 SV=6	K1C10_HUMAN	59 kDa	334	320	302
	Keratin, type I cytoskeletal 16 OS=Homo sapiens GN=KRT16 PE=1 SV=4	K1C16_HUMAN	51 kDa	129	158	142
	Keratin, type I cytoskeletal 14 OS=Homo sapiens GN=KRT14 PE=1 SV=4	K1C14_HUMAN	52 kDa	149	155	144
	Keratin, type I cytoskeletal 17 OS=Homo sapiens GN=KRT17 PE=1 SV=2	K1C17_HUMAN	48 kDa	90	94	70
	Keratin, type I cuticular Ha1 OS=Homo sapiens GN=KRT31 PE=2 SV=3	K1H1_HUMAN	47 kDa	11	17	8
	Keratin, type I cuticular Ha3-I OS=Homo sapiens GN=KRT33A PE=2 SV=2	KT33A_HUMAN	46 kDa	10	0	8
	Keratin, type I cuticular Ha6 OS=Homo sapiens GN=KRT36 PE=1 SV=1	KRT36_HUMAN	52 kDa	2	6	6
	Keratin, type I cytoskeletal 23 OS=Homo sapiens GN=KRT23 PE=1 SV=2	K1C23_HUMAN	48 kDa	0	2	3
	Keratin, type II cytoskeletal 1 OS=Homo sapiens GN=KRT1 PE=1 SV=6	K2C1_HUMAN	66 kDa	448	649	504
	Keratin, type II cytoskeletal 2 epidermal OS=Homo sapiens GN=KRT2 PE=1 SV=2	K22E_HUMAN	65 kDa	254	265	240
	Keratin, type II cytoskeletal 5 OS=Homo sapiens GN=KRT5 PE=1 SV=3	K2C5_HUMAN	62 kDa	123	145	114
	Keratin, type II cytoskeletal 6B OS=Homo sapiens GN=KRT6B PE=1 SV=5	K2C6B_HUMAN	60 kDa	110	156	107
	Keratin, type II cytoskeletal 6A OS=Homo sapiens GN=KRT6A PE=1 SV=3	K2C6A_HUMAN	60 kDa	117	132	73
	Keratin, type II cytoskeletal 8 OS=Homo sapiens GN=KRT8 PE=1 SV=7	K2C8_HUMAN	54 kDa	144	129	53
	Keratin, type II cytoskeletal 7 OS=Homo sapiens GN=KRT7 PE=1 SV=5	K2C7_HUMAN	51 kDa	55	64	30
	Keratin, type II cytoskeletal 6C OS=Homo sapiens GN=KRT6C PE=1 SV=3	K2C6C_HUMAN	60 kDa	26	28	35
	Keratin, type II cytoskeletal 1b OS=Homo sapiens GN=KRT77 PE=2 SV=3	K2C1B_HUMAN	62 kDa	7	13	27
	Keratin, type II cytoskeletal 80 OS=Homo sapiens GN=KRT80 PE=1 SV=2	K2C80_HUMAN	51 kDa	25	22	26
	Keratin, type II cytoskeletal 4 OS=Homo sapiens GN=KRT4 PE=1 SV=4	K2C4_HUMAN	57 kDa	28	22	25
	Keratin, type II cytoskeletal 78 OS=Homo sapiens GN=KRT78 PE=2 SV=2	K2C78_HUMAN	57 kDa	13	18	17
	Keratin, type II cuticular Hb3 OS=Homo sapiens GN=KRT83 PE=1 SV=2	KRT83_HUMAN	54 kDa	0	11	11
	Keratin, type II cuticular Hb5 OS=Homo sapiens GN=KRT85 PE=1 SV=1	KRT85_HUMAN	56 kDa	12	16	9
	Keratin, type II cytoskeletal 72 OS=Homo sapiens GN=KRT72 PE=1 SV=2	K2C72_HUMAN	56 kDa	17	9	8
	Keratin, type II cytoskeletal 2 oral OS=Homo sapiens GN=KRT76 PE=1 SV=2	K22O_HUMAN	66 kDa	0	9	5
	Keratin-81-like protein KRT121P OS=Homo sapiens GN=KRT121P PE=5 SV=4	K121P_HUMAN	29 kDa	9	11	8
	Desmoplakin OS=Homo sapiens GN=DSP PE=1 SV=3	DESP_HUMAN	332 kDa	77	124	95
	Sjoegren syndrome/scleroderma autoantigen 1 OS=Homo sapiens GN=SSSCA1 PE=1 SV=1	SSA27_HUMAN	21 kDa	0	0	193
	Desmoglein-1 OS=Homo sapiens GN=DSG1 PE=1 SV=2	DSG1_HUMAN	114 kDa	56	59	46
	Junction plakoglobin OS=Homo sapiens GN=JUP PE=1 SV=3	PLAK_HUMAN	82 kDa	39	36	22
	Hornerin OS=Homo sapiens GN=HRNR PE=1 SV=2	HORN_HUMAN	236 kDa	19	32	28
	Filaggrin-2 OS=Homo sapiens GN=FLG2 PE=1 SV=1	FILA2_HUMAN	242 kDa	15	22	21
	Desmocollin-1 OS=Homo sapiens GN=DSC1 PE=1 SV=2	DSC1_HUMAN	100 kDa	15	21	18
	Suprabasin OS=Homo sapiens GN=SBSN PE=2 SV=2	SBSN_HUMAN	61 kDa	5	9	12
	Dermcidin OS=Homo sapiens GN=DCD PE=1 SV=2	DCD_HUMAN	11 kDa	12	12	8
	Plakophilin-1 OS=Homo sapiens GN=PKP1 PE=1 SV=2	PKP1_HUMAN	83 kDa	4	5	4
	Corneodesmosin OS=Homo sapiens GN=CDSN PE=1 SV=3	CDSN_HUMAN	52 kDa	6	9	6
Cytoskeletal Proteins	Tubulin beta chain OS=Homo sapiens GN=TUBB PE=1 SV=2	TBB5_HUMAN	50 kDa	111	142	64
	Tubulin beta-4B chain OS=Homo sapiens GN=TUBB4B PE=1 SV=1	TBB4B_HUMAN	50 kDa	113	134	58
	Tubulin beta-4A chain OS=Homo sapiens GN=TUBB4A PE=1 SV=2	TBB4A_HUMAN	50 kDa	0	0	32
	Tubulin alpha-1C chain OS=Homo sapiens GN=TUBA1C PE=1 SV=1	TBA1C_HUMAN	50 kDa	93	101	38
	Tubulin alpha-1B chain OS=Homo sapiens GN=TUBA1B PE=1 SV=1	TBA1B_HUMAN	50 kDa	29	0	38
	Annexin A2 OS=Homo sapiens GN=ANXA2 PE=1 SV=2	ANXA2_HUMAN	39 kDa	22	20	16
	Cofilin-1 OS=Homo sapiens GN=CFL1 PE=1 SV=3	COF1_HUMAN	19 kDa	9	15	10
	Serine/threonine-protein kinase PAK 1 OS=Homo sapiens GN=PAK1 PE=1 SV=2	PAK1_HUMAN	61 kDa	2	9	6
	Profilin-1 OS=Homo sapiens GN=PFN1 PE=1 SV=2	PROF1_HUMAN	15 kDa	2	4	3
RNPs	Heterogeneous nuclear ribonucleoprotein U OS=Homo sapiens GN=HNRNPU PE=1 SV=6	HNRPU_HUMAN	91 kDa	50	46	25
	Heterogeneous nuclear ribonucleoprotein D-like OS=Homo sapiens GN=HNRPDL PE=1 SV=3	HNRDL_HUMAN	46 kDa	2	4	2
	40S ribosomal protein S3 OS=Homo sapiens GN=RPS3 PE=1 SV=2	RS3_HUMAN	27 kDa	26	20	11
	40S ribosomal protein S3a OS=Homo sapiens GN=RPS3A PE=1 SV=2	RS3A_HUMAN	30 kDa	10	4	7
	40S ribosomal protein S9 OS=Homo sapiens GN=RPS9 PE=1 SV=3	RS9_HUMAN	23 kDa	6	6	4
	40S ribosomal protein S26 OS=Homo sapiens GN=RPS26 PE=1 SV=3	RS26_HUMAN	13 kDa	6	4	4
	60S ribosomal protein L27a OS=Homo sapiens GN=RPL27A PE=1 SV=2	RL27A_HUMAN	17 kDa	13	10	8
	60S ribosomal protein L9 OS=Homo sapiens GN=RPL9 PE=1 SV=1	RL9_HUMAN	22 kDa	17	10	9
	60S ribosomal protein L17 OS=Homo sapiens GN=RPL17 PE=1 SV=3	RL17_HUMAN	21 kDa	14	8	10
	60S ribosomal protein L19 OS=Homo sapiens GN=RPL19 PE=1 SV=1	RL19_HUMAN	23 kDa	14	8	14
	60S ribosomal protein L10 OS=Homo sapiens GN=RPL10 PE=1 SV=4	RL10_HUMAN	25 kDa	12	10	7
	60S ribosomal protein L13 OS=Homo sapiens GN=RPL13 PE=1 SV=4	RL13_HUMAN	24 kDa	7	3	4
	Putative RNA-binding protein Luc7-like 2 OS=Homo sapiens GN=LUC7L2 PE=1 SV=2	LC7L2_HUMAN	47 kDa	4	1	2
Mitochondrial	Mitochondrial inner membrane protein OS=Homo sapiens GN=IMMT PE=1 SV=1	IMMT_HUMAN	84 kDa	0	0	105
	Coiled-coil-helix-coiled-coil-helix domain-containing protein 3, mitochondrial OS=Homo sapiens GN=CHCHD3 I	CHCH3_HUMAN	26 kDa	0	0	32
	Metaxin-2 OS=Homo sapiens GN=MTX2 PE=1 SV=1	MTX2_HUMAN	30 kDa	0	0	12
	Arginase-1 OS=Homo sapiens GN=ARG1 PE=1 SV=2	ARGI1_HUMAN	35 kDa	13	9	8
	ATP synthase subunit alpha, mitochondrial OS=Homo sapiens GN=ATP5A1 PE=1 SV=1	ATPA_HUMAN	60 kDa	7	2	4
Cytoplasmic	Glyceraldehyde-3-phosphate dehydrogenase OS=Homo sapiens GN=GAPDH PE=1 SV=3	G3P_HUMAN	36 kDa	18	24	21
	Pyruvate kinase isozymes M1/M2 OS=Homo sapiens GN=PKM PE=1 SV=4	KPYM_HUMAN	58 kDa	22	25	18
	Alpha-enolase OS=Homo sapiens GN=ENO1 PE=1 SV=2	ENOA_HUMAN	47 kDa	21	11	18
	Protein-glutamine gamma-glutamyltransferase E OS=Homo sapiens GN=TGM3 PE=1 SV=4	TGM3_HUMAN	77 kDa	12	13	9
	Protein-glutamine gamma-glutamyltransferase K OS=Homo sapiens GN=TGM1 PE=1 SV=4	TGM1_HUMAN	90 kDa	3	1	3
	Bleomycin hydrolase OS=Homo sapiens GN=BLMH PE=1 SV=1	BLMH_HUMAN	53 kDa	2	1	6
	Fructose-bisphosphate aldolase A OS=Homo sapiens GN=ALDOA PE=1 SV=2	ALDOA_HUMAN	39 kDa	4	2	2
Nuclear	Probable ATP-dependent RNA helicase DDX5 OS=Homo sapiens GN=DDX5 PE=1 SV=1	DDX5_HUMAN	69 kDa	14	20	10
	ATP-dependent RNA helicase DDX3X OS=Homo sapiens GN=DDX3X PE=1 SV=3	DDX3X_HUMAN	73 kDa	16	17	8
	Histone H4 OS=Homo sapiens GN=HIST1H4A PE=1 SV=2	H4_HUMAN	11 kDa	19	10	13
	Histone H2B type 2-E OS=Homo sapiens GN=HIST2H2BE PE=1 SV=3	H2B2E_HUMAN	14 kDa	8	3	8
	Histone H2B type 3-B OS=Homo sapiens GN=HIST3H2BB PE=1 SV=3	H2B3B_HUMAN	14 kDa	0	0	3
	Poly(U)-binding-splicing factor PUF60 OS=Homo sapiens GN=PUF60 PE=1 SV=1	PUF60_HUMAN	60 kDa	12	3	6
Other	Serum albumin OS=Homo sapiens GN=ALB PE=1 SV=2	ALBU_HUMAN	69 kDa	9	11	12
	Sorting and assembly machinery component 50 homolog OS=Homo sapiens GN=SAMM50 PE=1 SV=3	SAM50_HUMAN	52 kDa	0	0	29
	Serpin B12 OS=Homo sapiens GN=SERPINB12 PE=1 SV=1	SPB12_HUMAN	46 kDa	6	9	8
	Tankyrase-1 OS=Homo sapiens GN=TNKS PE=1 SV=2	TNKS1_HUMAN	142 kDa	0	0	19
	Tankyrase-2 OS=Homo sapiens GN=TNKS2 PE=1 SV=1	TNKS2_HUMAN	127 kDa	0	0	2
	L-lactate dehydrogenase A chain OS=Homo sapiens GN=LDHA PE=1 SV=2	LDHA_HUMAN	37 kDa	4	3	9
	L-lactate dehydrogenase B chain OS=Homo sapiens GN=LDHB PE=1 SV=2	LDHB_HUMAN	37 kDa	1	1	3
	UPF0444 transmembrane protein C12orf23 OS=Homo sapiens GN=C12orf23 PE=1 SV=1	CL023_HUMAN	12 kDa	5	5	6
	E3 ubiquitin-protein ligase HERC2 OS=Homo sapiens GN=HERC2 PE=1 SV=2	HERC2_HUMAN	527 kDa	0	0	8
	Catalase OS=Homo sapiens GN=CAT PE=1 SV=3	CATA_HUMAN	60 kDa	0	7	4
	Peptidyl-prolyl cis-trans isomerase A OS=Homo sapiens GN=PPIA PE=1 SV=2	PPIA_HUMAN	18 kDa	5	1	3
	Cathepsin D OS=Homo sapiens GN=CTSD PE=1 SV=1	CATD_HUMAN	45 kDa	7	2	4
	Neuralized-like protein 4 OS=Homo sapiens GN=NEURL4 PE=1 SV=2	NEUL4_HUMAN	167 kDa	0	0	4
	Glutathione S-transferase P OS=Homo sapiens GN=GSTP1 PE=1 SV=2	GSTP1_HUMAN	23 kDa	2	2	2
	Prolactin-inducible protein OS=Homo sapiens GN=PIP PE=1 SV=1	PIP_HUMAN	17 kDa	1	0	4
	Protein POF1B OS=Homo sapiens GN=POF1B PE=1 SV=3	POF1B_HUMAN	68 kDa	0	1	4
	Prohibitin OS=Homo sapiens GN=PHB PE=1 SV=1	PHB_HUMAN	30 kDa	4	0	3
	Ig gamma-1 chain C region OS=Homo sapiens GN=IGHG1 PE=1 SV=1	IGHG1_HUMAN	36 kDa	4	2	2
	Gamma-glutamylcyclotransferase OS=Homo sapiens GN=GGCT PE=1 SV=1	GGCT_HUMAN	21 kDa	3	0	3

Supplemental Table S2. Proteins eliminated as contaminants in co-isolates with GFP nanobodies attached to magnetic beads. These proteins were present in EGFP-only affinity isolates at spectral count levels ≥ 50% of the number of peptides identified in EGFP-hSV or EGFP-anillin fractions.

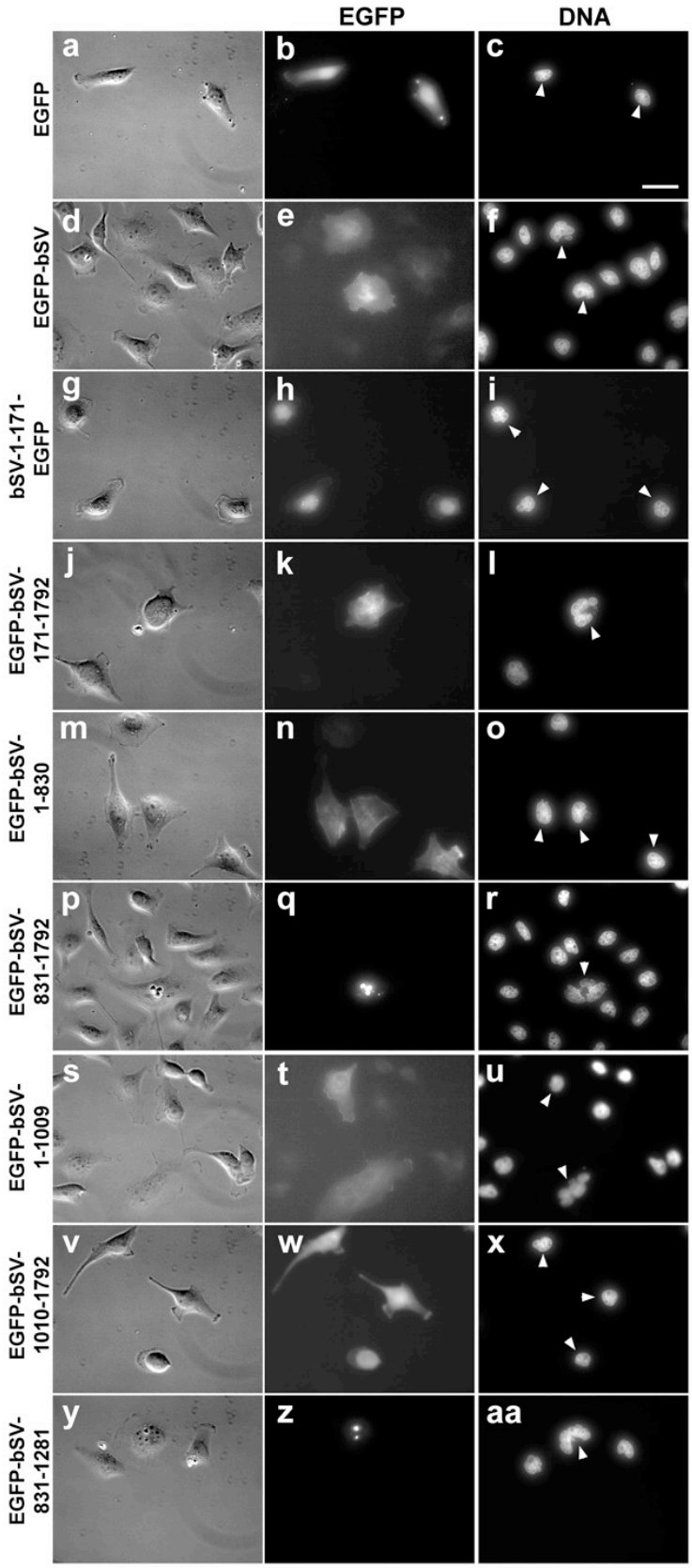

Supplemental Figure S1. Representative micrographs of interphase cells reported in Figure 1G. Cells were transfected with the indicated EGFP-tagged bovine supervillin constructs for 48 h and evaluated for bi/multinucleate phenotype. Phase images (a, d, g, j, m, p, s, v, y), EGFP (b, e, h, k, n, q, t, w, z), and DNA (c, f, i, l, o, r, u, x, aa). Nuclei of cells expressing EGFP-tagged proteins are indicated with white arrowheads (c, f, i, l, o, r, u, x, aa). Bar = 20 μm.

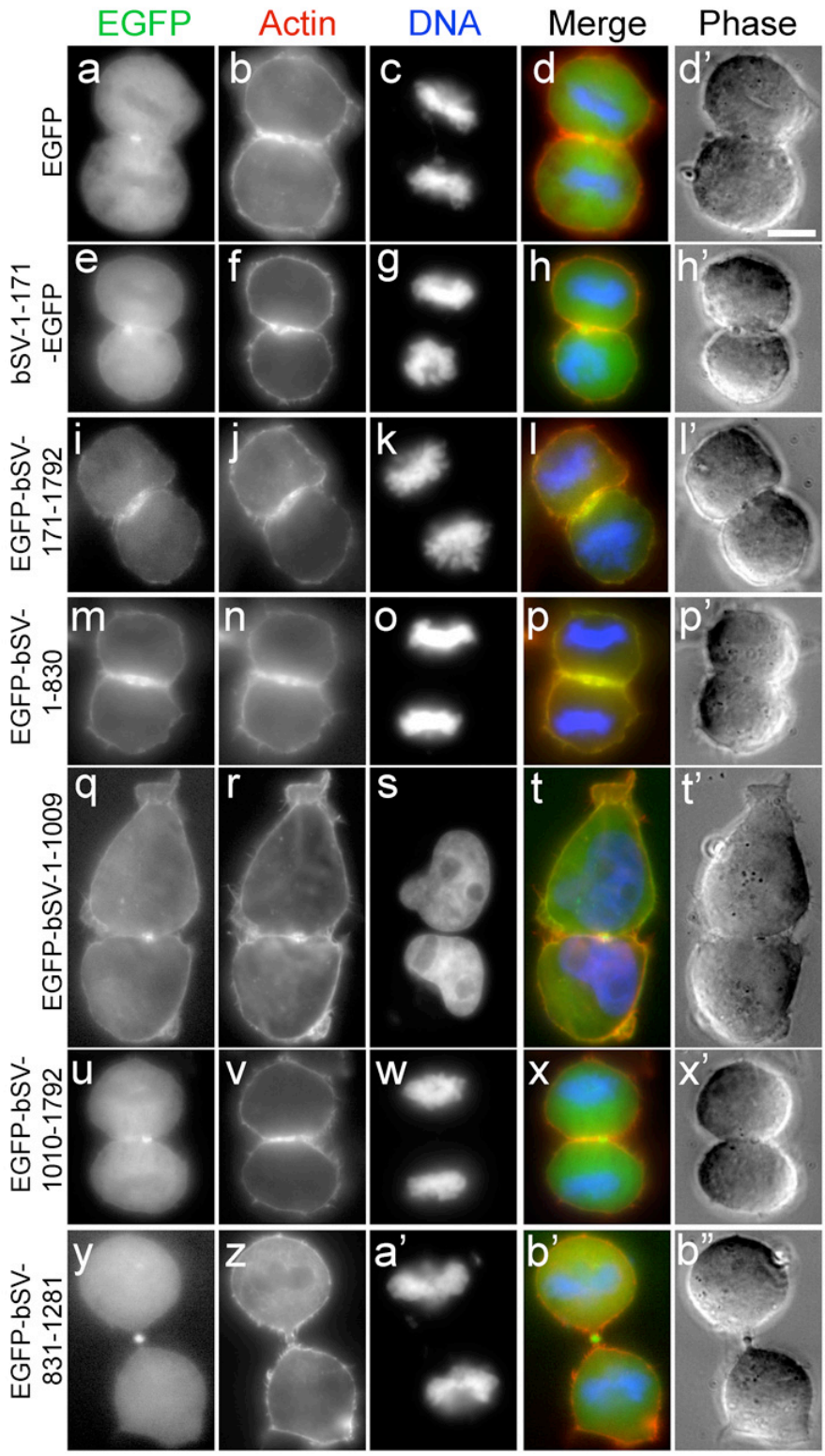

Supplemental Figure S2. Representative localizations of EGFP-tagged supervillin deletion constructs in dividing cells. EGFP (a-d), bSV-1-171-EGFP (e-h), EGFP-bSV-171-1792 (i-l), EGFP-bSV-1-830 (m-p), EGFP-bSV-1-1009 (q-t), EGFP-bSV-1010-1792 (u-x), and EGFP-bSV-831 - 1281 (y-b'). EGFP (green in merges) shown in a, e, i, m, q, u, and y. Actin (red in merges) shown in b, f, j, n, r, v, and z. DNA (blue in merges), c, g, k, o, s, w, and a'. Merged images in d, h, l, p, t, x, and b'. Phase images in d', h', l', p', t', x', b". Bar = 10 μm.

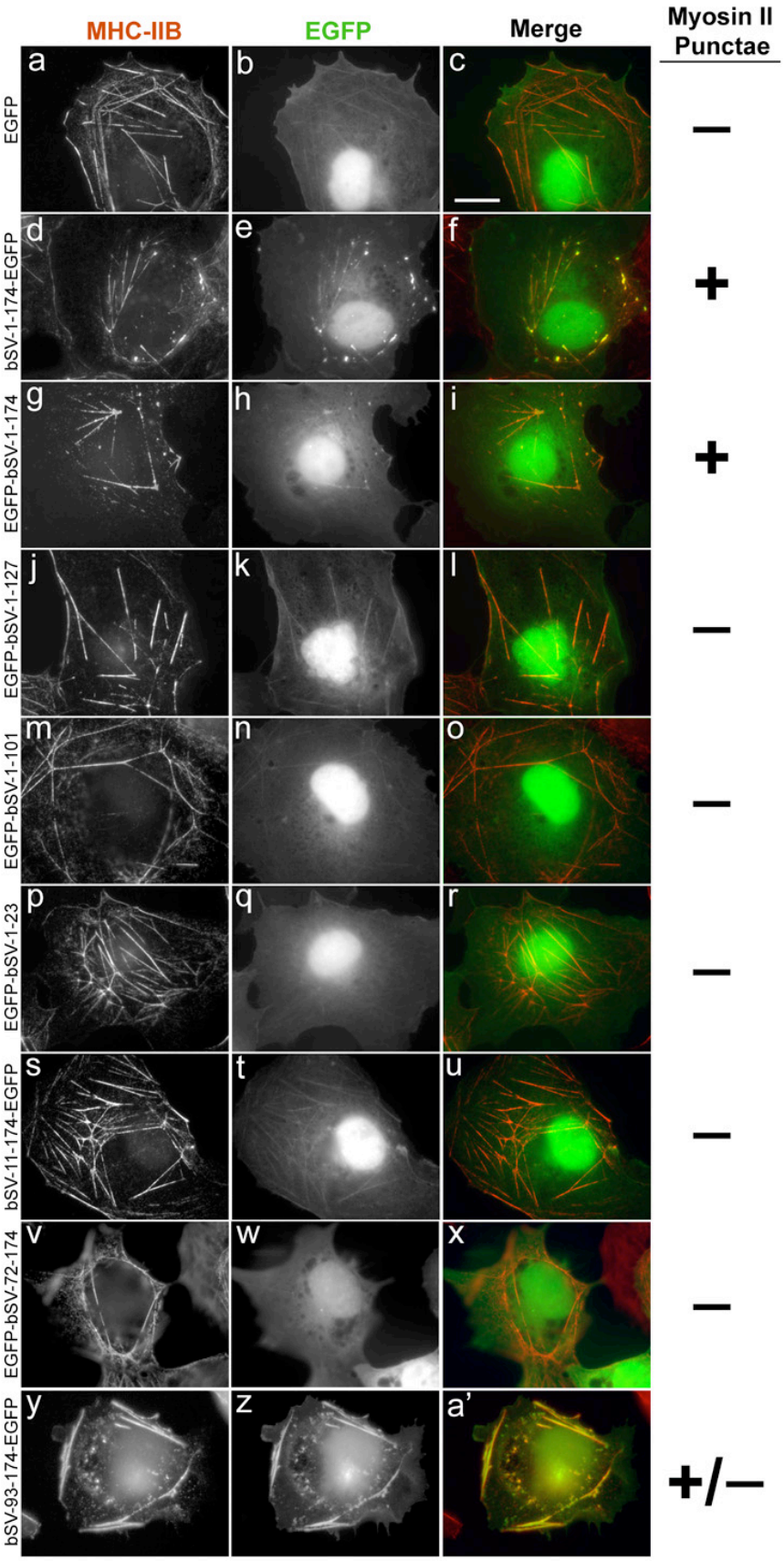

Supplemental Figure S3. Representative micrographs showing the effects of deletion mutations within bSV-1-174-EGFP on the ability of this protein to form myosin II punctae after overexpression in COS7 cells. EGFP-tagged full-length bSV-1-174 causes hyperactivation of co-localizing myosin II filaments into stable punctae with L-MLCK (Chen *et al.*, 2003; Takizawa *et al.*, 2007). Transfected COS7 cells were stained for myosin IIB heavy chain (MHC-IIB; a, d, g, j, m, p, s, v, y; red in merges) and evaluated for myosin II punctae, indicated at right by (+) punctae formed, (+/-) incomplete conversion, or (-) no punctae. EGFP constructs (b, e, h, k, n, q, t, w, z; green in merges) are: (b) EGFP alone, (e) bSV-1-174-EGFP, (h) EGFP-bSV-1-174, (k) EGFP-bSV-1-127, (n) EGFP-bSV-1-101, (q) EGFP-bSV-1-23, (t) bSV-11-174-EGFP, (w) EGFP-bSV-72-174, and (z) bSV-93-174-EGFP. Merged images (c, f, i, l, o, r, u, x, a'). Bar, 20 µm.

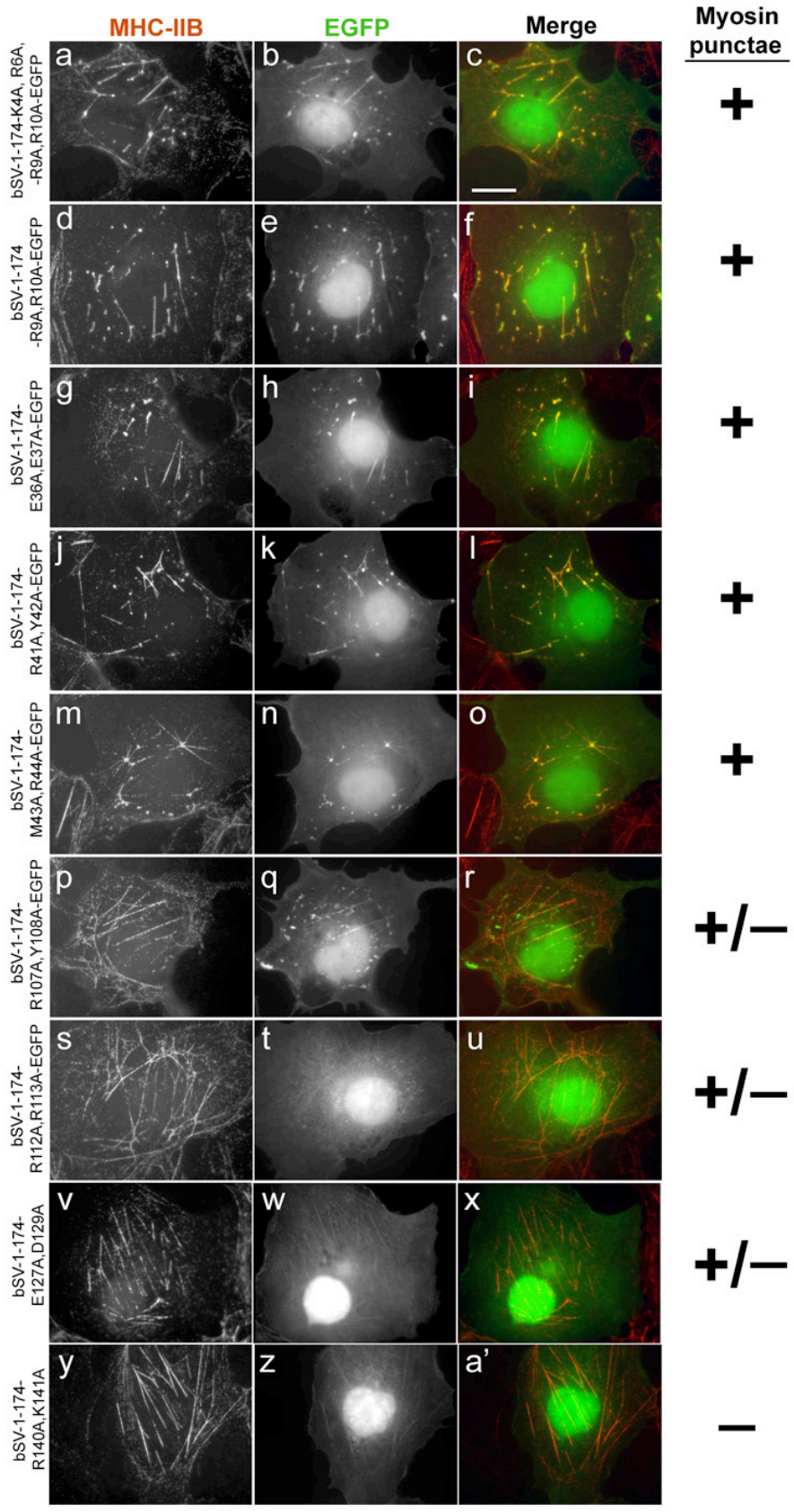

Supplemental Figure S4. Representative micrographs showing the effects of point mutations within bSV-1-174-EGFP on the ability of this protein to form hyperactivated myosin II punctae after overexpression in COS7 cells. Transfected COS7 cells were stained for myosin II heavy chain (a, d, g, j, m, p, s, v, y; red in merges) and evaluated for myosin II-punctae, indicated at right by (+) punctae formed, (+/-) incomplete conversion, and (-) no punctae. EGFP constructs (b, e, h, k, n, q, t, w, z; green in merges) are: (b) bSV-1-174-K4A,R6A,R9A,R10A-EGFP; (e) bSV-1-174-R9A,R10A-EGFP; (h) bSV-1-174-E36A,E37A-EGFP; (k) bSV-1-174-R41A,Y42A-EGFP; (n) bSV-1-174-M43A,R44A-EGFP; (q) bSV-1-174-R107A,Y108A-EGFP; (t) bSV-1-174-R112A,R113A-EGFP; (w) BSV-1-174-EGFP-E127A,D129A; (z), BSV-1-174-EGFP-R140A,K141A. Merged images (c, f, i, l, o, r, u, x, a'). Bar, 20 µm.

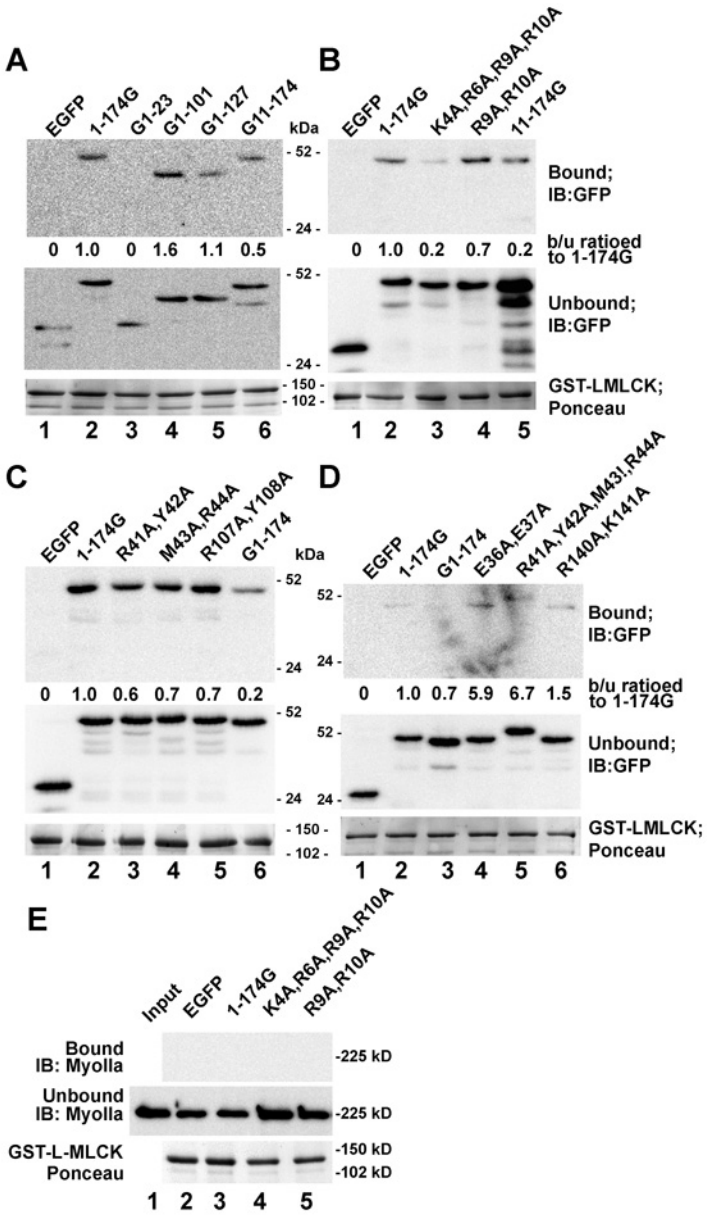

Supplemental Figure S5. Identification of supervillin sequences required for L-MLCK interaction. (A, B, C, D) Bound and unbound deletion and point mutants of EGFP-tagged bSV 1-174, as indicated, in pulldown experiments with the GST-tagged L-MLCK N-terminus. Blots were probed with anti-GFP; Ponceau staining of blots with bound proteins shows equal loading of the GST-tagged bait protein. Ratios of bound:unbound EGFP signal, normalized to 1-174-EGFP ratio, are shown. Ratios ≤ 0.5 were considered to indicate reduction in binding to L-MLCK. $N \geq 2$. (E) Immunoblot of bound and unbound fractions probed for MHC-IIA in cell lysates. Input lysate (lane 1), EGFP (lane 2), bSV-1-174-EGFP (lane 3), bSV-1-174-K4A,R6A,R9A,R10A-EGFP (lane 4), bSV-1-174-R9A,R10A-EGFP (lane 5). Bound and unbound samples were probed on the same blot; Ponceau staining shows GST-L-MLCK-6Ig in bound fractions to verify loading.